aerospace

MDPI

Article

Adaptive Spatial Cooperative Guidance for Impact-Speed Coordination and Two-Phase Inter-Vehicle Separation

Shuai Yuan [1], Zhanpeng Gao [2] and Wenjun Yi [2,*]

[1] School of Energy and Power Engineering, Nanjing University of Science and Technology, Nanjing 210094, China
[2] National Key Lab of Transient Physics, Nanjing University of Science and Technology, Nanjing 210094, China
* Correspondence: wenjunyi@njust.edu.cn

Abstract

Safe cooperative interception must coordinate arrival, terminal geometry, closing speed, and internal spacing at the same time. This study formulates a spatial cooperative guidance scheme that couples range synchronization, terminal relative-speed regulation, adaptive transverse convergence, and active separation among interceptors. Along the line of sight (LOS), finite-time agreement of range-related states is superposed with a shared closing-speed servo, thereby separating the difference dynamics inside the multi-vehicle system from the mean radial-speed mode. In the two angular channels, the constant reaching gain is replaced with a time-, range-, and error-dependent gain that moderates the initial command peak while preserving terminal LOS-angle convergence. Collision risk is handled in two phases. During the early trajectory-reshaping phase, a smoothed neighbor-repulsion command is projected onto the transverse plane so that the radial speed loop is not perturbed. After the LOS-angle errors enter the assigned band, separated terminal approach directions are used to avoid late trajectory aggregation. Numerical tests show that the scheme removes early overload saturation and increases the minimum spacing while keeping the terminal constraints. In three deterministic cases, the terminal angle errors are on the order of 10^{-6}, the relative impact-speed errors are on the order of 10^{-3}, and the miss distances are approximately 0.8 m. Two 200-run Monte Carlo tests with launch-condition perturbations and measurement noise give terminal angle errors on the order of 10^{-3}, relative impact-speed errors around 0.5 m/s, and miss distances concentrated near 0.5 m. These results indicate that the proposed design improves command smoothness and spacing performance without sacrificing cooperative terminal accuracy under the tested engagement conditions.

Keywords: adaptive control; multi-vehicle coordination; sliding mode guidance; angle constraint

Check for updates

Academic Editor: Konstantinos Kontis

Received: 16 June 2026
Revised: 19 August 2026
Accepted: 20 August 2026
Published: 21 August 2026

Copyright: © 2026 by the authors. Licensee MDPI, Basel, Switzerland. This article is an open access article distributed under the terms and conditions of the Creative Commons Attribution (CC BY) license.

1. Introduction

Modern cooperative interception is shaped by several coupled requirements rather than by terminal homing alone. Multiple vehicles must arrive in a coordinated manner, respect the prescribed approach geometry, regulate the closing-speed condition, and retain enough spacing between neighboring trajectories. These requirements become especially entangled when the target maneuvers or when the launch layout is compact. Cooperative guidance has therefore become an important approach for improving engagement reliability and mission redundancy in multi-interceptor systems [1]. Its value is particularly evident

against fast maneuvering targets, where a single interceptor may not provide a sufficient performance margin [2,3].

Recent reviews place cooperative guidance in a broader systems context. Feng et al. [4] surveyed game-theoretic approaches to cooperation and competition in multi-agent systems, while Yang et al. [5] reviewed trajectory-planning methods for high-speed vehicles under physical, computational, and implementation constraints.

Most existing coordination strategies can be viewed through the variable selected for synchronization. Some designs synchronize geometric, terminal-angle, or prescribed-time cooperative variables [6,7], whereas another group drives the estimated time-to-go (tgo) toward agreement [8,9]. These approaches aim at a simultaneous strike, but they allocate the longitudinal channel differently and interact with terminal-angle control in different ways.

For tgo-based cooperation, many designs force the estimates carried by different vehicles to approach a shared value [10]. Since the accuracy of tgo prediction directly affects impact-time regulation, prediction-based impact-time guidance has also been studied for practical anti-ship guided-vehicle engagements [11]. Guo et al. [12] used directed information exchange to build coupled longitudinal and normal-direction commands for impact-angle-constrained cooperative attack. Zhao et al. [13] coordinated several interceptors through a leader–follower arrangement. These studies establish useful cooperative architectures, but many of them assume stationary targets or simplified geometries. For maneuvering targets, Zhang et al. [14] introduced biased proportional navigation guidance (PNG) to satisfy impact-angle requirements in anti-ship guided-vehicle scenarios. Zhang et al. [15] separated the process into a finite-time consensus stage and a terminal angle-control stage. Related two-dimensional cooperative guidance designs were further reported in [16,17]. However, planar engagement models do not fully represent the spatial coupling between LOS inclination, LOS declination, radial motion, and inter-vehicle separation in realistic three-dimensional encounters.

Spatial cooperative guidance has consequently attracted sustained attention [18]. A recent knowledge-graph review by Liu et al. [19] summarized this field in terms of relative-motion models, graph-theoretic tools, cooperative structures, and convergence properties. Wang et al. [20] combined proportional navigation with a two-stage cooperative scheme for specified impact-angle attack. Chang et al. [21] assigned the longitudinal coordination to a consensus law and synthesized the angular commands through optimal-control arguments. Wang et al. [22] also studied distributed three-dimensional guidance with specified impact-angle constraints. Beyond cooperative settings, Li et al. [23] recently derived a near-optimal impact-vector-control law from three-dimensional nonlinear kinematics, showing how terminal direction shaping can be connected with energy-efficient guidance. Prescribed-time spatial cooperation has also been advanced by fully distributed designs that combine LOS-direction impact-time consensus with prescribed-performance LOS-angle control against maneuvering targets [24]. These studies clarify how terminal geometry and convergence-time requirements can be embedded into spatial guidance, but they usually treat the internal spacing of the multi-vehicle system as a secondary issue rather than as a guidance constraint to be actively managed. The present study does not treat impact-angle satisfaction, prescribed or specified arrival time, or terminal-speed regulation as separate novelties, nor does it directly prescribe an impact time. Instead, cooperative arrival is achieved through remaining-range consensus and common relative impact-speed regulation. On this basis, inter-vehicle spacing is treated as an active guidance variable and integrated with terminal-angle constraints, cooperative arrival, and relative impact-speed regulation within a three-dimensional guidance framework.

Geometric and suboptimal impact-time/impact-angle formulations provide another route to terminal timing control [25,26]. In cooperative interception, range-to-go or leader–

follower variables can then be used so that the vehicles reach the target consistently. Zhou et al. [27] used range-to-go coordination together with adaptive estimation of target maneuvers. Li et al. [28] made the follower's range-to-go track that of the leader while maintaining the desired impact angle. Nevertheless, the dominant objective in these works remains cooperative arrival or terminal-angle satisfaction. The safety problem inside the multi-vehicle system has received less explicit attention, although collision avoidance is a basic requirement in other cooperative motion systems, including marine vessels [29,30] and unmanned aerial vehicles [31,32]. Safety-aware cooperative-guidance studies have begun to address this gap more directly. Chen et al. [33] coordinated polynomial reference trajectories through a safe-distance criterion while imposing terminal flight-path-angle conditions, whereas Chen et al. [34] used a second-order control barrier function to convert spatial threat-area constraints into online restrictions for cooperative penetration. The former embeds collision avoidance in reference-trajectory parameterization, and the latter enforces a safety constraint through an optimization-compatible barrier condition. The present method instead separates the internal inter-vehicle safety task by engagement phase: a LOS-transverse repulsive bias reshapes nearby trajectories before angular convergence, and vehicle-specific terminal LOS directions provide directional deconfliction afterward, while the radial arrival- and speed-coordination channel is left unchanged.

For a multi-vehicle cooperative engagement, internal safety is difficult to guarantee by terminal-angle design alone. Adjacent vehicles may start from nearby launch points, and rapid trajectory correction can further reduce their separation before the terminal geometry has converged. A guidance law that ignores this transient interaction may achieve accurate interception while still producing an unacceptable close-encounter risk. The design problem is therefore to increase the inter-vehicle distance margin without weakening cooperative arrival or terminal accuracy.

The longitudinal channel also influences the practical value of a cooperative attack. Terminal impact velocity is often treated as a terminal-state requirement in penetration and cooperative guidance studies [35,36]. Increasing terminal speed is useful only if the resulting commands remain smooth enough for the interceptor to execute. Time-varying velocity and impact-velocity constraints have therefore been considered in guidance design [36–41]. Learning-based and constraint-rich cooperative laws further broaden this setting to variable maneuvering targets and LOS- or overload-related limitations [42–45]. Nevertheless, early command peaks or overload saturation can still limit practical implementation when terminal timing, angle, and velocity requirements are imposed together. Such saturation can erode the stability and reliability that cooperative guidance is intended to provide.

The present work also differs from the fault-accommodation study in [35]. There, the main specifications are relative impact speed and attack angle in the presence of fault-related requirements. Here, the design is reorganized around two additional operating issues: excessive early command demand and unsafe spacing between neighboring vehicles. The LOS-direction speed loop is therefore combined with a transverse two-phase safety mechanism since a cooperative engagement may meet its terminal speed and angle specifications while still experiencing a close encounter during the approach.

From a verification perspective, recent reliability studies have combined physical information, monitoring data, or surrogate models to assess reliability and uncertainty under complex or data-limited conditions [46–48]. These studies motivate the explicit evaluation of guidance sensitivity over prescribed perturbation ranges in the present work. However, this study neither constructs a surrogate reliability model nor estimates failure probabilities; instead, its Monte Carlo tests introduce launch-state perturbations, target-state perturbations, and measurement noise.

The close-encounter risk considered here comes from compact initial deployment, rapid transverse reshaping, and late aggregation of approach directions. The proposed design responds to these two risk windows separately. In the first window, neighboring interceptors are regarded as moving obstacles, and a smoothed repulsive term is injected only into the transverse command after its LOS-radial component is removed. Thus, range cooperation and relative impact-speed regulation remain decoupled from the avoidance action. In the second window, once the terminal LOS-angle error is sufficiently small, different terminal approach directions maintain the final separation pattern. In parallel, an adaptive reaching law is introduced in the LOS normal and lateral channels to reduce peak overload during early convergence. The LOS direction contains both range consensus and common relative-speed regulation, so the multi-vehicle system can coordinate arrival while driving the group closing speed toward the prescribed value.

The specific advances are listed below:

1. The paper introduces a separation mechanism matched to the two dominant close-encounter phases. The early transverse repulsion enlarges the distance between nearby vehicles without changing the LOS-direction speed-coordination loop, whereas the late differentiated terminal-angle arrangement reduces same-direction aggregation near impact. This extends the cooperative guidance setting in [43,49–53] from terminal coordination alone to simultaneous terminal coordination and distance-margin regulation.
2. For the LOS normal and lateral channels, the reaching gain is scheduled by time, sliding-state magnitude, and remaining range. This scheduling softens the initial transverse command and restores stronger convergence as the engagement proceeds. Compared with recent designs that emphasize overload saturation, time-varying velocity, impact velocity, learning-based coordination, or multiple physical constraints [35,36,38,39,41–45], the proposed form targets early-stage overload saturation without relaxing the terminal angle requirement.
3. The resulting framework integrates range consensus, common relative impact-speed regulation, adaptive transverse convergence, and two-phase separation in a spatial engagement model. Ablation simulations, comparisons with appointed-time and fixed-time terminal-angle guidance laws, extended initial-distance tests, and Monte Carlo tests were conducted to evaluate terminal accuracy, command behavior, and inter-vehicle spacing.

The rest of the manuscript proceeds as follows. Section 2 formulates the engagement model and the safety issue. Section 3 derives the cooperative controller and the two-phase separation term. Section 4 reports the numerical verification. Section 5 gives the concluding remarks and future work.

2. Problem Description and Guidance Model

2.1. Inter-Vehicle Close-Encounter Risk and Stage-Based Treatment

In a cooperative engagement, synchronized arrival and terminal LOS-angle accuracy do not automatically guarantee safe spacing inside the multi-vehicle system. When the initial formation is tight, aggressive trajectory reshaping can shrink the distance between adjacent vehicles before the terminal geometry has settled. Inter-vehicle separation is therefore introduced as an additional safety objective coupled with the guidance task.

The risk mechanism is illustrated in Figure 1. At the beginning of the engagement, different launch points, target maneuver, and rapid trajectory correction can produce complex relative motion inside the multi-vehicle system. If two neighboring vehicles are initially close, the transient correction process may cause their trajectories to intersect or pass within an unsafe distance. Later in the engagement, after the cooperative states have

nearly converged, another risk appears when several vehicles approach the target from similar directions. In that case, terminal trajectory aggregation can again reduce the spacing before impact.

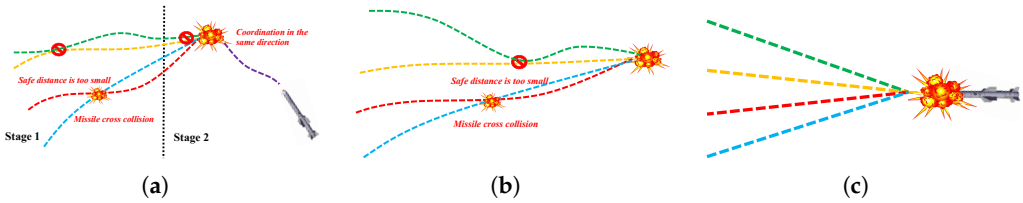


Figure 1. Schematic of inter-vehicle close-encounter risk and stage-based treatment in cooperative guidance. (**a**) Two-stage close-encounter risk in cooperative guidance; (**b**) first-stage repulsive-bias collision avoidance; (**c**) second-stage differentiated terminal LOS-angle constraints. Note: Green, yellow, blue, and red dashed curves denote interceptor trajectories, and the purple dashed curve denotes the target trajectory. Explosion and prohibition symbols indicate collision or interception points and unsafe spacing, respectively.

These observations motivate a stage-based treatment. Before the terminal LOS-angle error converges, the dominant threat is a transient close encounter caused by initial deployment and trajectory reshaping. Neighboring vehicles are therefore modeled as dynamic obstacles, and a collision-avoidance bias is injected only into the normal and lateral channels after removing its LOS-radial component. Once the angle error falls inside the prescribed threshold, the dominant threat changes to terminal approach aggregation. The cooperative formation then relies on differentiated terminal LOS-angle constraints to keep the final approach directions separated.

The two stages therefore serve different roles. The repulsive bias enlarges the distance margin during the early transient, whereas the differentiated terminal angles reduce same-direction convergence near the target. Combining these mechanisms gives the inter-vehicle distance regulation strategy used in this paper.

2.2. Inter-Vehicle Communication Topology

The multi-vehicle information network is modeled as an undirected weighted graph $G = (\varepsilon, \xi, \tau)$. Each node in ε corresponds to one vehicle, and ε_i denotes the i-th vehicle. The edge set ξ identifies the vehicle pairs that exchange cooperative information, while τ collects the associated weights. For each undirected edge, $w_{ij} = w_{ji} > 0$ denotes its weight. Following [54], the adjacency entries are

$$a_{ij} = \begin{cases} w_{ij}, & \{\varepsilon_i, \varepsilon_j\} \in \xi \\ 0, & \text{otherwise.} \end{cases} \tag{1}$$

Let N denote the number of vehicles. Let $\mathcal{L} = [l_{ij}] \in \mathcal{R}^{N\times N}$ be the graph Laplacian. The diagonal entry records the total weight incident on node i, whereas the off-diagonal entry is the negative edge weight:

$$l_{ij} = \begin{cases} \sum\limits_{t=1, t\neq i}^{N} a_{it}, & j = i \\ -a_{ij}, & j \neq i \end{cases} \tag{2}$$

Lemma 1 ([55]). *For a second-order multi-agent system over an undirected connected graph, the following consensus input yields finite-time agreement:*

$$u_i = -\gamma_1 \sum_{l=1}^{N} a_{il} \operatorname{sig}^{a_1}(x_{1i} - x_{1l}) - \gamma_2 \sum_{l=1}^{N} a_{il} \operatorname{sig}^{\frac{2a_1}{1+a_1}}(x_{2i} - x_{2l}) \tag{3}$$

where a_{il} is the graph weight, $\gamma_1 > 0$, $\gamma_2 > 0$, $0 < a_1 < 1$, and $\operatorname{sig}^{a_1}(x) = |x|^{a_1} \operatorname{sgn}(x)$. Since $a_{il} = a_{li}$ for an undirected graph and both $\operatorname{sig}^{a_1}(\cdot)$ and $\operatorname{sig}^{\frac{2a_1}{1+a_1}}(\cdot)$ are odd, all pairwise terms vanish after summing over the multi-vehicle system, namely, $\sum_{i=1}^{N} u_i = 0$. Thus, the consensus term modifies only the relative states among vehicles. It does not alter the group-average radial velocity, which allows a common impact-speed regulator to be added in the LOS-direction channel.

Consistent with Lemma 1, the subsequent analysis considers a fixed, undirected, connected communication graph with synchronous neighbor-state exchange.

2.3. Vehicle–Target Model

Figure 2 gives the relative geometry adopted in the model. The inertial frame is $OXYZ$, and the target and vehicle body-related frames are $OX_TY_TZ_T$ and $OX_MY_MZ_M$. For the vehicle or target, $\theta_{M/T}$ denotes flight-path elevation, and $\phi_{M/T}$ denotes flight-path azimuth. The LOS frame $OX_LY_LZ_L$ uses θ_L, ϕ_L, and R to describe LOS inclination, LOS declination, and vehicle-target range.

For the convenience of analysis, the following assumptions are made:

Assumption 1 ([56]). *To accommodate different engagement scenarios, the vehicle speed is assumed to be greater than the target speed.*

Assumption 2 ([57]). *The vehicle autopilot is assumed to be ideal, with no response delay.*

Assumption 3 ([58]). *The vehicle velocity direction is aligned with the vehicle body axis, i.e., the angle of attack is zero.*

Assumption 4 ([36,45]). *The vehicle has speed-control authority. Different from conventional boost–glide vehicles, the interceptor considered in this paper is powered by a sustainer engine, such as a turbojet or ramjet engine, which allows active thrust modulation and thus enables precise control of the vehicle–target relative closing speed.*

Assumption 5 ([59]). *During the guidance process, the LOS inclination angle always avoids the singular position. That is, there exists a constant $c_\theta > 0$ such that $|\cos\theta_{L,i}(t)| \geq c_\theta$, $\forall t \in [0, T_f)$, $i = 1, 2, \ldots, N$, thereby avoiding the singularity caused by the term $1/\cos\theta_{L,i}$ in the LOS lateral dynamics.*

These assumptions define the operating range of the guidance-layer model. The speed advantage in Assumption 1 provides a positive closing margin; if this margin cannot be maintained, interception and the prescribed relative impact speed are not guaranteed. Assumption 2 treats the commanded accelerations as accurately realized, whereas appreciable autopilot lag, limited bandwidth, or actuator saturation may slow LOS-angle convergence and reduce the spacing margin. Under Assumption 3, the body axis is aligned with the vehicle velocity direction. For a moving target, the absolute vehicle flight-path angles characterize the inertial velocity direction, whereas the LOS angles characterize the relative vehicle–target geometry. Assumption 4 requires active thrust authority and therefore applies to powered interceptors rather than purely ballistic or unpowered vehicles. Assumption 5 keeps the LOS coordinates away from singularity; if this condition is approached, a nonsingular LOS representation is required before evaluating the lateral command.

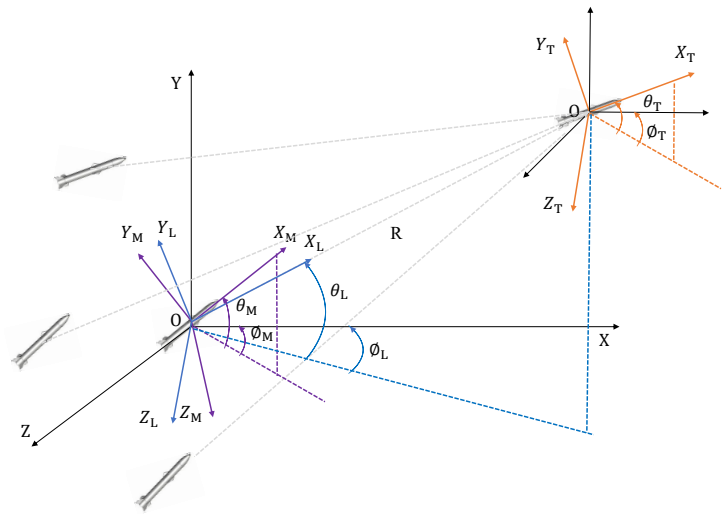


Figure 2. Vehicle–target relative motion geometry.

From this geometry, the vehicle–target relative motion can be written as [30]

$$\ddot{R}_i = R_i\left(\dot{\theta}_{L,i}^2 + \dot{\phi}_{L,i}^2 \cos^2\theta_{L,i}\right) + a_{Tr,i} - a_{Mr,i} \tag{4}$$

$$\ddot{\theta}_{L,i} = -\frac{2\dot{R}_i}{R_i}\dot{\theta}_{L,i} - \dot{\phi}_{L,i}^2 \cos\theta_{L,i}\sin\theta_{L,i} + \frac{1}{R_i}\left(a_{T\theta,i} - a_{M\theta,i}\right) \tag{5}$$

$$\ddot{\phi}_{L,i} = \dot{\phi}_{L,i}\left(-\frac{2\dot{R}_i}{R_i} + 2\dot{\theta}_{L,i}\tan\theta_{L,i}\right) - \frac{1}{R_i\cos\theta_{L,i}}\left(a_{T\phi,i} - a_{M\phi,i}\right) \tag{6}$$

where $[a_{M/Tr,i}, a_{M/T\theta,i}, a_{M/T\phi,i}]$ are the interceptor/target acceleration components resolved in the LOS coordinate system. The centroid kinematics of the vehicle and target are

$$\begin{cases} \dot{X}_{M/T,i} = V_{M/T,i}\cos\theta_{M/T,i}\cos\phi_{M/T,i} \\ \dot{Y}_{M/T,i} = V_{M/T,i}\sin\theta_{M/T,i} \\ \dot{Z}_{M/T,i} = -V_{M/T,i}\cos\theta_{M/T,i}\sin\phi_{M/T,i} \end{cases} \tag{7}$$

$$\begin{cases} \dot{\theta}_{M/T,i} = \dfrac{a_{M/Ty,i}}{V_{M/T,i}} \\ \dot{\phi}_{M/T,i} = -\dfrac{a_{M/Tz,i}}{V_{M/T,i}\cos\theta_{M/T,i}} \end{cases} \tag{8}$$

where $[a_{M/Tx,i}, a_{M/Ty,i}, a_{M/Tz,i}]$ are the interceptor/target acceleration components in the ballistic coordinate system. The transformation from the ballistic frame to the LOS frame is [60]

$$T(\theta_L, \phi_L) = \begin{bmatrix} \cos\theta_L\cos\phi_L & \sin\theta_L & -\cos\theta_L\sin\phi_L \\ -\sin\theta_L\cos\phi_L & \cos\theta_L & \sin\theta_L\sin\phi_L \\ \sin\phi_L & 0 & \cos\phi_L \end{bmatrix} \tag{9}$$

$$T(\theta_M, \phi_M) = \begin{bmatrix} \cos\theta_M\cos\phi_M & \sin\theta_M & -\cos\theta_M\sin\phi_M \\ -\sin\theta_M\cos\phi_M & \cos\theta_M & \sin\theta_M\sin\phi_M \\ \sin\phi_M & 0 & \cos\phi_M \end{bmatrix} \tag{10}$$

2.4. Guidance Model

Combining centroid kinematics with the vehicle–target relative-motion equations separates the multi-vehicle system dynamics into LOS-direction, LOS-normal, and LOS-

lateral parts. To encode the desired impact geometry, define $x_{1i} = R_i$, $x_{2i} = \dot{R}_i$, $x_{3i} = \theta_{L,i} - \theta_{\exp,i}$, $x_{4i} = \dot{\theta}_{L,i}$, $x_{5i} = \phi_{L,i} - \phi_{\exp,i}$, and $x_{6i} = \dot{\phi}_{L,i}$.

The LOS-direction dynamics take the form

$$\begin{cases} \dot{x}_{1i} = x_{2i} \\ \dot{x}_{2i} = x_{1i}\left(x_{4i}^2 + x_{6i}^2 \cos^2\theta_{L,i}\right) + a_{Tr,i} - a_{Mr,i} \end{cases} \tag{11}$$

The normal-direction angular dynamics are

$$\begin{cases} \dot{x}_{3i} = x_{4i} \\ \dot{x}_{4i} = -\dfrac{2x_{2i}}{x_{1i}} x_{4i} - x_{6i}^2 \cos\theta_{L,i} \sin\theta_{L,i} + \dfrac{1}{x_{1i}}(a_{T\theta,i} - a_{M\theta,i}) \end{cases} \tag{12}$$

The lateral-direction angular dynamics are

$$\begin{cases} \dot{x}_{5i} = x_{6i} \\ \dot{x}_{6i} = x_{6i}\left(-\dfrac{2x_{2i}}{x_{1i}} + 2x_{4i}\tan\theta_{L,i}\right) - \dfrac{1}{x_{1i}\cos\theta_{L,i}}\left(a_{T\phi,i} - a_{M\phi,i}\right) \end{cases} \tag{13}$$

Here, $\theta_{\exp}$ and $\phi_{\exp}$ are the desired LOS inclination and declination angles. Their ordered pair prescribes the terminal relative-approach direction through the unit vector $\hat{l}_{\exp,i} = [\cos\theta_{\exp,i}\cos\phi_{\exp,i},\ \sin\theta_{\exp,i},\ -\cos\theta_{\exp,i}\sin\phi_{\exp,i}]^{\mathrm{T}}$. As $R_i \to 0$ and the two LOS rates converge to zero, the terminal relative-velocity direction aligns with this LOS vector. Thus, the two desired LOS components jointly define the three-dimensional relative impact geometry. For a moving target, the corresponding absolute vehicle flight-path angles additionally depend on the target velocity and are therefore distinguished from this relative terminal geometry. Accordingly, the terminal-angle constraint considered below is the terminal LOS-angle constraint. The controller is then assigned three tasks. The LOS-direction channel must reduce differences in range and radial velocity while also regulating the group-average closing speed to $V_{\exp}$. The normal and lateral channels must drive the LOS-angle errors and their rates to small terminal neighborhoods so that the prescribed terminal LOS-angle constraints are met. These requirements are expressed as

$$\begin{cases} \lim\limits_{t\to T_f} x_{1i} = 0, \quad \lim\limits_{t\to T_f} x_{2i} = V_{\exp} \\ \lim\limits_{t\to T_f} (x_{1i} - x_{1j}) = 0, \quad \lim\limits_{t\to T_f} (x_{2i} - x_{2j}) = 0, \quad i,j = 1,2,\ldots,N \\ \lim\limits_{t\to T_f} x_{3i} = 0, \quad \lim\limits_{t\to T_f} x_{4i} = 0 \\ \lim\limits_{t\to T_f} x_{5i} = 0, \quad \lim\limits_{t\to T_f} x_{6i} = 0 \end{cases} \tag{14}$$

where T_f is the actual vehicle flight time and $V_{\exp} < 0$ is the commanded vehicle-target relative impact speed. The required speed is assumed to lie within the vehicle speed-control capability.

3. Controller Synthesis

The controller is built by assigning different roles to the radial and angular channels. Target-acceleration estimates are supplied by the fractional-power extended state observer (FPESO) adopted from [35,61]. The radial command handles range agreement and the common impact-speed loop, while the two angular commands enforce terminal LOS angles

and carry the separation bias. This channel allocation allows terminal accuracy, speed coordination, and inter-vehicle spacing to be handled within one structure.

3.1. LOS-Normal Channel Design

The LOS-normal channel controls the inclination-angle error. The corresponding state dynamics are

$$\begin{cases} \dot{x}_{3i} = x_{4i} \\ \dot{x}_{4i} = -\dfrac{2x_{2i}}{x_{1i}} x_{4i} - x_{6i}^2 \cos\theta_{L,i} \sin\theta_{L,i} + \dfrac{1}{x_{1i}} (a_{T\theta,i} - a_{M\theta,i}) \end{cases} \tag{15}$$

Choose the sliding manifold

$$s_{2i} = x_{4i} - \frac{2n_1 \dot{R}_i}{R_i} x_{3i} + \frac{k_s}{R_i^{n_1}} x_{3i} \tag{16}$$

where $n_1 > 0$ schedules how the angle-error feedback strengthens as R_i decreases, and $k_s > 0$ is the feedback gain. Differentiation gives

$$\dot{s}_{2i} = \dot{x}_{4i} - \frac{2n_1 \ddot{R}_i}{R_i} x_{3i} + \frac{2n_1 \dot{R}_i^2}{R_i^2} x_{3i} - \frac{2n_1 \dot{R}_i}{R_i} x_{4i} + \frac{k_s}{R_i^{n_1}} x_{4i} - \frac{n_1 \dot{R}_i k_s}{R_i^{n_1+1}} x_{3i} \tag{17}$$

The term $\ddot{R}_i$ is not assumed to be directly measurable. It is included in the disturbance channel and is compensated through the observer estimate.

A fixed-gain reaching law provides a simple convergence mechanism, but it is poorly matched to the different phases of an engagement. Large values of b_1 and b_2 accelerate convergence at the cost of a large initial command, which may exceed actuator capability. Smaller gains reduce chattering and saturation, but they also delay the response to nonlinear coupling and target maneuver. The following reaching law is the fixed-gain baseline:

$$\dot{s} = -b_1 \operatorname{sig}^{q_1}(s) - b_2 \operatorname{sig}^{q_2}(s) \tag{18}$$

In the reaching law, $q_1 = \frac{m_1+1}{2} + \frac{m_1-1}{2} \operatorname{sgn}(|s| - 1)$, $q_2 = \frac{m_2+1}{2} - \frac{m_2-1}{2} \operatorname{sgn}(|s| - 1)$, where $m_1 > 1$, $\frac{1}{2} < m_2 < 1$, $b_j > 0$, $j = 1, 2$, and $\operatorname{sig}^{\rho}(s) = |s|^{\rho} \operatorname{sgn}(s)$ for $\rho > 0$.

To remove this phase mismatch, the reaching gain is scheduled by time, sliding-state magnitude, and remaining range. The adaptive factor $g(t, s_{2i}, R_i) \in (0, 1)$ is

$$g(t, s_{2i}, R_i) = \frac{1}{1 + \exp\left[-k_t(t - t_0) + k_p|s_{2i}| - k_R/R_i\right]} \tag{19}$$

Here, t denotes the physical guidance time measured continuously from guidance initiation. This physical clock remains continuous as the sliding state enters a local error region, and t_0 denotes a fixed transition time on the same clock. The parameters $k_t > 0$, $t_0 \geq 0$, $k_p > 0$, and $k_R > 0$ determine, respectively, the transition rate, the center of the soft-start interval, the sensitivity to the sliding variable, and the inverse-range activation strength. This structure keeps the initial transverse command moderate and increases the convergence authority as the engagement approaches the terminal phase.

The scheduled reaching dynamics are then

$$\dot{s}_{2i} = g(t, s_{2i}, R_i)(-b_1 \operatorname{sig}^{q_1}(s_{2i}) - b_2 \operatorname{sig}^{q_2}(s_{2i})) \tag{20}$$

Solving for the normal acceleration command yields

$$a_{M\theta,i} = x_{1i}\Bigg(-\frac{2x_{2i}}{x_{1i}}x_{4i} - x_{6i}^2\cos\theta_{L,i}\sin\theta_{L,i} + \frac{1}{x_{1i}}a_{T\theta,i} - \frac{2n_1\ddot{R}_i}{R_i}x_{3i} + \frac{2n_1\dot{R}_i^2}{R_i^2}x_{3i} - \frac{2n_1\dot{R}_i}{R_i}x_{4i} + \frac{k_s}{R_i^{n_1}}x_{4i} - \frac{n_1\dot{R}_i k_s}{R_i^{n_1+1}}x_{3i} - \dot{s}_{2i}\Bigg) \tag{21}$$

Theorem 1. *Consider the nominal continuous and unsaturated LOS-normal command in Equation (21), with exact observer compensation and an inactive separation bias. If $R_i(t) > 0$ and the sliding manifold is reached before interception, the LOS inclination angle of each vehicle converges to its prescribed terminal value.*

Use the Lyapunov candidate

$$V_{3i} = \frac{1}{2}s_{2i}^2 \tag{22}$$

Its derivative is

$$\dot{V}_{3i} = s_{2i}\dot{s}_{2i} = -g(t, s_{2i}, R_i)\left[b_1(2V_{3i})^{\frac{q_1+1}{2}} + b_2(2V_{3i})^{\frac{q_2+1}{2}}\right] \tag{23}$$

Because $q_2 = m_2 \in (0,1)$ for $|s_{2i}| < 1$, the lower-order term dominates as $V_{3i} \to 0$. Thus,

$$\dot{V}_{3i} \le -g(t, s_{2i}, R_i)b_2(2V_{3i})^{\frac{q_2+1}{2}} \tag{24}$$

Let

$$\gamma_a = \frac{q_2+1}{2}, \quad 0 < \gamma_a < 1 \tag{25}$$

Since the adaptive gain satisfies $g(t, s_{2i}, R_i) \in (0,1)$ and is continuous and bounded over the finite guidance interval, there exists a positive constant $g_{\min} > 0$ such that

$$g(t, s_{2i}, R_i) \ge g_{\min} \tag{26}$$

For $|s_{2i}| > 1$, $q_2 = 1$, and the linear b_2 term drives any finite initial state into $|s_{2i}| \le 1$ in finite time. Let $t_{e,i}$ denote this entry time on the physical guidance clock (or the guidance initial time if the state already lies in the small-error region), and introduce the local proof variable $\tau = t - t_{e,i}$. Hence, $\tau = 0$ marks entry into the local region, while the adaptive factor retains the continuous-time argument $t = t_{e,i} + \tau$ and is evaluated as $g(t_{e,i} + \tau, s_{2i}, R_i)$.

Let

$$C = b_2 2^{\gamma_a} g_{\min} \tag{27}$$

Then,

$$\dot{V}_{3i} \le -CV_{3i}^{\gamma_a}, \quad 0 < \gamma_a < 1 \tag{28}$$

Integrating the above inequality gives the finite-time convergence upper bound

$$T^* \le \frac{V_{3i}(t_{e,i})^{1-\gamma_a}}{C(1-\gamma_a)} = \frac{V_{3i}(t_{e,i})^{1-\frac{q_2+1}{2}}}{b_2 2^{\frac{q_2+1}{2}} g_{\min}\left(1-\frac{q_2+1}{2}\right)} \tag{29}$$

Combining the finite entry interval $t_{e,i}$ with the local-duration bound T^*, the sliding manifold s_{2i} reaches zero in finite physical time and remains there.

When the system converges to the sliding manifold, one has $x_{4i} = \frac{2n_1\dot{R}_i}{R_i}x_{3i} - \frac{k_s}{R_i^{n_1}}x_{3i}$. Construct the Lyapunov function as

$$V_{4i} = \frac{1}{2}x_{3i}^2 \tag{30}$$

Taking its derivative gives

$$\begin{aligned}\dot{V}_{4i} = x_{3i}\dot{x}_{3i} &= x_{3i}\left(\frac{2n_1\dot{R}_i}{R_i}x_{3i} - \frac{k_s}{R_i^{n_1}}x_{3i}\right) \\ &= \frac{2n_1\dot{R}_i}{R_i}x_{3i}^2 - \frac{k_s}{R_i^{n_1}}x_{3i}^2\end{aligned} \tag{31}$$

Since $\dot{R}_i$ is the relative flight velocity and is negative during the approaching process, $n_1 > 0$ and $k_s > 0$ are sufficient to guarantee system stability.

3.2. LOS-Lateral Channel Design

The lateral channel is treated in the same spirit, with the declination-angle error as the controlled variable. Its state dynamics are

$$\begin{cases}\dot{x}_{5i} = x_{6i} \\ \dot{x}_{6i} = x_{6i}\left(-\dfrac{2x_{2i}}{x_{1i}} + 2x_{4i}\tan\theta_{L,i}\right) - \dfrac{1}{x_{1i}\cos\theta_{L,i}}\left(a_{T\phi,i} - a_{M\phi,i}\right)\end{cases} \tag{32}$$

Select the sliding manifold

$$s_{3i} = x_{6i} - \frac{2n_1\dot{R}_i}{R_i}x_{5i} + \frac{k_s}{R_i^{n_1}}x_{5i} \tag{33}$$

Use the scheduled reaching dynamics

$$\dot{s}_{3i} = g(t, s_{3i}, R_i)(-b_1\,\mathrm{sig}^{q_1}(s_{3i}) - b_2\,\mathrm{sig}^{q_2}(s_{3i})) \tag{34}$$

The resulting lateral acceleration command is

$$\begin{aligned}a_{M\phi,i} = -x_{1i}\cos\theta_{L,i}\Bigg(x_{6i}\left[-\frac{2x_{2i}}{x_{1i}} + 2x_{4i}\tan\theta_{L,i}\right] - \frac{1}{x_{1i}\cos\theta_{L,i}}a_{T\phi,i} - \frac{2n_1\ddot{R}_i}{R_i}x_{5i} \\ + \frac{2n_1\dot{R}_i^2}{R_i^2}x_{5i} - \frac{2n_1\dot{R}_i}{R_i}x_{6i} + \frac{k_s}{R_i^{n_1}}x_{6i} - \frac{n_1\dot{R}_i k_s}{R_i^{n_1+1}}x_{5i} - \dot{s}_{3i}\Bigg)\end{aligned} \tag{35}$$

The lateral-channel proof follows the same Lyapunov argument used for the normal channel and is omitted for brevity.

3.3. LOS-Direction Channel Design

The radial channel is responsible for coordinating the remaining range and radial velocity while regulating the prescribed relative impact speed. The LOS-direction dynamics are

$$\begin{cases}\dot{x}_{1i} = x_{2i} \\ \dot{x}_{2i} = x_{1i}\left(x_{4i}^2 + x_{6i}^2\cos^2\theta_{L,i}\right) + a_{Tr,i} - a_{Mr,i}\end{cases} \tag{36}$$

where $x_{1i} = R_i$ and $x_{2i} = \dot{R}_i$. To handle range cooperation and relative impact-speed regulation simultaneously, the equivalent radial input is split into a difference-mode term and a common velocity-mode term:

$$u_{r,i} = u_{c,i} + u_v. \tag{37}$$

Here, $u_{c,i}$ suppresses the remaining-range and radial-velocity differences among vehicles, while u_v regulates the formation-level radial closing speed.

The inter-vehicle consensus term is chosen as

$$u_{c,i} = -\gamma_1 \sum_{l=1}^{N} a_{il} \operatorname{sig}^{a_1}(x_{1i} - x_{1l}) - \gamma_2 \sum_{l=1}^{N} a_{il} \operatorname{sig}^{\frac{2a_1}{1+a_1}}(x_{2i} - x_{2l}). \tag{38}$$

where $\gamma_1 > 0$, $\gamma_2 > 0$, and $0 < a_1 < 1$. This term forces both remaining-range and radial-velocity differences to vanish in finite time.

The formation-average radial velocity is

$$\bar{v}_R = \frac{1}{N} \sum_{i=1}^{N} x_{2i}. \tag{39}$$

The common velocity servo is

$$u_v = -k_v \operatorname{sig}^{\eta}(\bar{v}_R - V_{\exp}). \tag{40}$$

where $k_v > 0$, $0 < \eta < 1$, and $V_{\exp} < 0$ is the prescribed relative impact speed. Because u_v is identical for all vehicles, it acts only on the common velocity mode and does not change inter-vehicle relative states.

$$\dot{x}_{2i} = u_{c,i} + u_v. \tag{41}$$

The corresponding radial acceleration command is

$$a_{Mr,i} = x_{1i}\left(x_{4i}^2 + x_{6i}^2 \cos^2 \theta_{L,i}\right) + \hat{a}_{Tr,i} - u_{c,i} - u_v. \tag{42}$$

where $\hat{a}_{Tr,i}$ is the estimated target radial acceleration. If the target radial acceleration can be directly obtained, one may set $\hat{a}_{Tr,i} = a_{Tr,i}$. When estimation error exists, $a_{Tr,i} - \hat{a}_{Tr,i}$ can be regarded as a bounded residual disturbance, and its influence is verified in the subsequent simulations.

Theorem 2. *Suppose the communication graph is undirected and connected, and the target radial acceleration is exactly compensated, $\hat{a}_{Tr,i} = a_{Tr,i}$. Under the LOS-direction command in Equation (42), the multi-vehicle system reaches finite-time agreement in remaining range and radial velocity, and its average radial velocity converges to the prescribed relative impact speed $V_{\exp}$. If these convergences occur before interception, the vehicles hit the maneuvering target cooperatively with the required relative impact speed.*

Proof. Inserting the radial command into the LOS-direction dynamics gives

$$\begin{cases} \dot{x}_{1i} = x_{2i} \\ \dot{x}_{2i} = u_{c,i} + u_v. \end{cases} \tag{43}$$

First, examine the inter-vehicle difference mode. For any vehicles i and j,

$$\dot{x}_{2i} - \dot{x}_{2j} = u_{c,i} - u_{c,j}. \tag{44}$$

Because u_v is identical for all vehicles, it cancels from the difference dynamics. Hence, the convergence of remaining-range and radial-velocity differences is governed by $u_{c,i}$. Lemma 1 then guarantees that, for an undirected connected topology, there exists a finite time T_c such that, for $t \geq T_c$,

$$x_{1i} - x_{1j} = 0, \qquad x_{2i} - x_{2j} = 0, \qquad i, j = 1, 2, \ldots, N. \tag{45}$$

Thus, the multi-vehicle system reaches finite-time agreement in range and radial velocity. Next, for the common velocity mode, the definition of $\bar{v}_R$ gives

$$\dot{\bar{v}}_R = \frac{1}{N}\sum_{i=1}^{N} \dot{x}_{2i} = \frac{1}{N}\sum_{i=1}^{N}(u_{c,i} + u_v). \tag{46}$$

That is,

$$\dot{\bar{v}}_R = \frac{1}{N}\sum_{i=1}^{N} u_{c,i} + u_v. \tag{47}$$

Because the communication topology is undirected, satisfying $a_{il} = a_{li}$, and $\mathrm{sig}^a(\cdot)$ is an odd function, the pairwise consensus terms satisfy

$$\sum_{i=1}^{N} u_{c,i} = 0. \tag{48}$$

Therefore,

$$\dot{\bar{v}}_R = u_v. \tag{49}$$

Substituting the common velocity regulation term yields

$$\dot{\bar{v}}_R = -k_v \,\mathrm{sig}^{\eta}(\bar{v}_R - V_{\mathrm{exp}}). \tag{50}$$

Let

$$e_v = \bar{v}_R - V_{\mathrm{exp}}. \tag{51}$$

Then,

$$\dot{e}_v = -k_v \,\mathrm{sig}^{\eta}(e_v). \tag{52}$$

Choose the Lyapunov function

$$V_v = \frac{1}{2}e_v^2. \tag{53}$$

Taking its derivative gives

$$\dot{V}_v = e_v \dot{e}_v = -k_v |e_v|^{1+\eta}. \tag{54}$$

Since $0 < \eta < 1$, e_v converges to zero in finite time, and its convergence time satisfies

$$T_v \leq \frac{|e_v(0)|^{1-\eta}}{k_v(1-\eta)} = \frac{|\bar{v}_R(0) - V_{\mathrm{exp}}|^{1-\eta}}{k_v(1-\eta)}. \tag{55}$$

Thus, for $t \geq T_v$,

$$\bar{v}_R = V_{\mathrm{exp}}. \tag{56}$$

Combining the convergence of the difference mode and the common velocity mode, when

$$t \geq T_s = \max\{T_c, T_v\}, \tag{57}$$

one obtains

$$x_{1i} = x_{1j}, \qquad x_{2i} = x_{2j}, \qquad \bar{v}_R = V_{\exp}. \tag{58}$$

From $x_{2i} = x_{2j}$ and $\bar{v}_R = V_{\exp}$, it follows that

$$x_{2i} = V_{\exp}, \qquad i = 1, 2, \ldots, N. \tag{59}$$

At this stage, all vehicles share the same remaining range and radial closing speed. Since $V_{\exp} < 0$ and $x_{1i} = R_i$, the multi-vehicle system approaches the target from an identical radial state. If $T_s < T_f$, the actual interception moment satisfies

$$\lim_{t \to T_f} x_{1i} = 0, \qquad \lim_{t \to T_f} x_{2i} = V_{\exp}. \tag{60}$$

Therefore, cooperative interception is achieved with the required relative impact speed. The proof is complete. □

It should be emphasized that Theorems 1 and 2 describe the finite-time convergence mechanisms of the nominal model. Acceleration saturation, FPESO estimation residuals, and measurement noise in practical implementation are not included in the preceding finite-time proofs; their effects are examined through the numerical simulations in Section 4. Thus, the theoretical analysis and numerical results are used, respectively, to establish nominal convergence and to assess closed-loop performance in the presence of these non-ideal factors.

3.4. Two-Phase Separation Strategy

The LOS-direction channel already contains the difference-mode term $u_{c,i}$ and the common speed term u_v. Directly adding an avoidance acceleration to this channel would disturb the average-speed loop. The separation action is therefore restricted to the normal and lateral channels. Let p_i, p_j, and $p_{t,i}$ be the inertial positions of vehicle i, neighboring vehicle j, and the target, respectively. Define $s_{ij} = p_i - p_j$, $d_{ij} = \|s_{ij}\|$, $\hat{s}_{ij} = s_{ij}/d_{ij}$, and $\hat{l}_i = (p_{t,i} - p_i)/\|p_{t,i} - p_i\|$. When $d_{ij} < d_{\text{warn}}$, the following distance-dependent repulsive acceleration is applied away from the neighbor:

$$a_{\text{rep},i} = \sum_{j \neq i} k_{\text{rep}} f_{ij} \max\left(\frac{1}{d_{ij}} - \frac{1}{d_{\text{warn}}}, 0\right)^{\beta} \hat{s}_{ij} \tag{61}$$

In this expression, $k_{\text{rep}} > 0$ sets the overall repulsive intensity. The amplification factor $f_{ij} = 1 + \gamma \exp[-(d_{ij}/d_{\text{warn}})^{\mu}]$ increases the avoidance command as the two vehicles become closer, where $\gamma > 0$ scales the near-range amplification and $\mu > 0$ shapes its decay. The exponent $\beta > 0$ determines how sharply the repulsive term grows inside the warning region.

Only the component orthogonal to the LOS is retained. In this way, the vehicles bypass one another transversely while the radial closing-speed loop remains intact. The projected command is $a_{\perp,i} = a_{\text{rep},i} - (a_{\text{rep},i} \cdot \hat{l}_i)\hat{l}_i$. Because the controller is expressed in the LOS frame whereas the repulsive term is computed from inertial positions, the projected command is transformed into the LOS coordinate system before saturation and implementation.

Near the warning radius, the transverse bias may change rapidly. A smooth saturation function is therefore applied to the normal and lateral avoidance components:

$$\tilde{a}_{\theta,i} = a_{\max} g_0 \tanh\left(\frac{\hat{a}_{\theta,i}}{p_s g_0}\right), \quad \tilde{a}_{\phi,i} = a_{\max} g_0 \tanh\left(\frac{\hat{a}_{\phi,i}}{p_s g_0}\right) \tag{62}$$

where $a_{\max}$ limits the bias acceleration and p_s sets the smoothness of the saturation. Here, g_0 denotes gravitational acceleration.

$$\widetilde{a} = \begin{cases} a_{\max} g_0 \tanh\left(\dfrac{\hat{a}}{p_s g_0}\right), & \dfrac{(|x_{3i}| + |x_{5i}|)180}{2\pi} \geq D_1 \\ 0, & \dfrac{(|x_{3i}| + |x_{5i}|)180}{2\pi} < D_1 \end{cases} \tag{63}$$

Once the LOS-angle errors fall inside the prescribed switching band, each vehicle is already tracking its assigned terminal LOS direction closely. The repulsive bias is then removed, and the late-stage mode relies on the differentiated direction assignments to avoid collapse onto a common final approach direction. The normal and lateral commands with the avoidance bias are

$$\begin{cases} a_{M\theta,i} = x_{1i}\Bigg(-\dfrac{2x_{2i}}{x_{1i}} x_{4i} - x_{6i}^2 \cos\theta_{L,i} \sin\theta_{L,i} + \dfrac{1}{x_{1i}} a_{T\theta,i} - \dfrac{2n_1 \ddot{R}_i}{R_i} x_{3i} + \dfrac{2n_1 \dot{R}_i^2}{R_i^2} x_{3i} \\ \qquad - \dfrac{2n_1 \dot{R}_i}{R_i} x_{4i} + \dfrac{k_s}{R_i^{n_1}} x_{4i} - \dfrac{n_1 \dot{R}_i k_s}{R_i^{n_1+1}} x_{3i} - \dot{s}_{2i} \Bigg) + \widetilde{a}_{\theta,i} \\ a_{M\phi,i} = -x_{1i} \cos\theta_{L,i} \Bigg(x_{6i} \left[-\dfrac{2x_{2i}}{x_{1i}} + 2x_{4i} \tan\theta_{L,i} \right] - \dfrac{1}{x_{1i} \cos\theta_{L,i}} a_{T\phi,i} - \dfrac{2n_1 \ddot{R}_i}{R_i} x_{5i} \\ \qquad + \dfrac{2n_1 \dot{R}_i^2}{R_i^2} x_{5i} - \dfrac{2n_1 \dot{R}_i}{R_i} x_{6i} + \dfrac{k_s}{R_i^{n_1}} x_{6i} - \dfrac{n_1 \dot{R}_i k_s}{R_i^{n_1+1}} x_{5i} - \dot{s}_{3i} \Bigg) + \widetilde{a}_{\phi,i} \end{cases} \tag{64}$$

The repulsive bias is used here to enlarge the inter-vehicle distance margin for the studied cooperative configurations. All six pairwise distances are monitored in the deterministic cases and the Monte Carlo analysis. It should not be interpreted as a formal global safety certificate for arbitrary multi-neighbor encounters. More rigorous safety-preserving conditions under multi-neighbor coupling conditions will be studied in future work through constrained optimization or related safety-filter methods.

3.5. Numerical Setup

The simulations use the vehicle and target initial conditions in Table 1.

Table 1. Initial states used in the numerical cases.

	M1	**M2**	**M3**	**M4**	**Target**
Position (m)	(1000, 0, 0)	(200, 1000, 0)	(−200, 0, 100)	(−400, 1000, 0)	(11,136, 8603.6, 5192.8)
V_M (m/s)	600	580	620	640	300
$\theta_{M/T}$ (°)	45	50	40	40	30
$\phi_{M/T}$ (°)	0	0	0	0	160
$\theta_{\exp}$ (°)	20	30	40	50	/
$\phi_{\exp}$ (°)	−40	−30	−20	−10	/

The four terminal LOS-angle pairs in Table 1 were prescribed offline as representative terminal commands for the numerical study. In an operational application, mission-specified terminal LOS directions can be supplied to the same controller, subject to kinematic feasibility and mutual distinction. The staggered inclination–declination pairs used here assign a different three-dimensional relative-approach vector to each vehicle. After the switching band is entered and the repulsive bias is removed, continued tracking of these distinct vectors provides directional deconfliction during the second stage. Together, the early distance-based repulsion and the differentiated terminal directions address the close-encounter risks that dominate the early and late stages of the engagement.

The controller and observer parameters are summarized in Table 2.

Table 2. Controller and observer parameter values.

Parameter	Value	Parameter	Value
m_1	$\frac{9}{7}$	m_2	$\frac{7}{9}$
b_1	1.5	b_2	1.5
n_1	0.8	k_s	50
k_t	1	k_p	2
k_R	0.1	t_0	10 s
γ_1	1	γ_2	0.5
a_1	0.78	D_1	5°
g_0	9.81 m/s^2	p_s	40
γ	0.2	k_{rep}	5×10^{16}
d_{warn}	200 m	β	5.4
μ	2	V_{exp}	−800 m/s

Table 3 summarizes the local tuning effects implied by Equation (19).

Table 3. Local tuning effects of the adaptive gain in Equation (19).

Parameter	Main Role	Effect When Increased	Main Trade-Off
k_t	Transition rate	Steeper change about t_0	Faster late rise
t_0	Transition time	Shifts the gain rise later	Later correction
k_p	Error weighting	Lowers g for large $\lvert s \rvert$	Lower peak; slower large-error decay
k_R	Inverse-range weighting	Raises g as R_i decreases	Stronger late correction

To represent actuator capability, the acceleration command is saturated at $30g_0$. Parameters without explicitly shown physical units are treated as dimensionless tuning constants. The target performs a serpentine maneuver with $a_{Tx} = 4g_0 \sin(0.2t)$, $a_{Ty} = 4g_0 \sin(0.2t)$, and $a_{Tz} = 4g_0 \cos(0.2t)$. The communication topology used by the multi-vehicle system is shown in Figure 3.

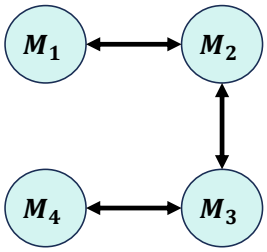


Figure 3. Communication topology.

4. Numerical Verification

The numerical study is organized as an ablation sequence followed by a benchmark comparison and Monte Carlo tests. The first case keeps the impact-speed loop but removes both adaptive reaching and separation. The second case introduces the adaptive reaching factor to examine early overload reduction. The third case activates the two-phase separation term to test whether the distance margin increases while terminal speed and angle accuracy are retained. The final tests compare three guidance laws, examine longer initial distances, and evaluate launch- or target-state perturbations together with measurement noise.

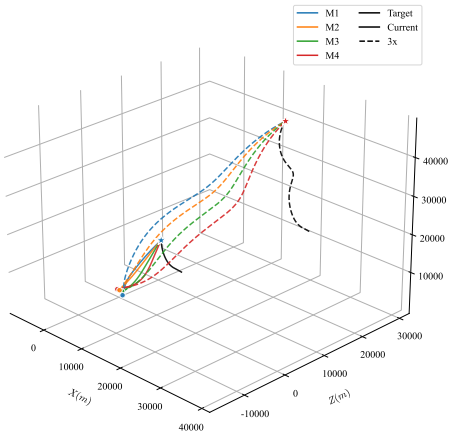
In terminal guidance, the controller does not set the engagement duration independently. For a fixed closing-speed setting and encounter geometry, it is governed mainly by the initial vehicle–target distance. Therefore, the deterministic results presented below include both the nominal condition and a three-times-distance condition. This extends the

displayed engagement from about 18–20 s to approximately 55 s without changing the controller structure, terminal constraints, or acceleration limit.

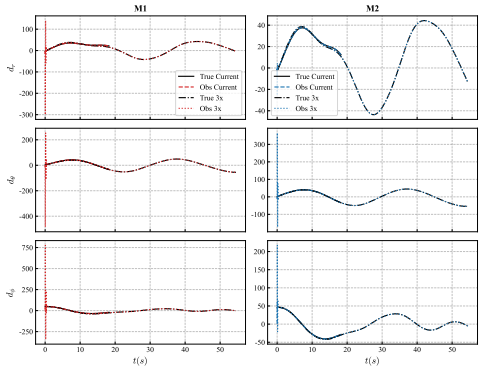
4.1. Baseline with Impact-Speed Regulation

In the first case, the adaptive reaching factor and the separation term are both disabled. In Figure 4, solid curves denote the nominal condition and dashed curves denote the three-times-distance condition. As shown in Figure 4, the FPESO exhibits an initial transient, but the estimated target acceleration quickly approaches the true acceleration in Figure 4b,c. The trajectory and terminal-state histories in Figure 4a,e,f verify coordinated interception with the assigned approach angles and the desired relative impact speed. The weakness appears in Figure 4d, where the LOS-normal and LOS-lateral acceleration commands saturate early in the engagement. This saturation increases actuator burden and can reduce implementation reliability. Moreover, Figure 4f shows that the spacing between Vehicle 3 and Vehicle 4 becomes very small, indicating that terminal accuracy is obtained with an insufficient internal safety margin. Under the three-times-distance condition, the early overload saturation and insufficient inter-vehicle spacing remain, indicating that extending the engagement duration does not eliminate these problems.

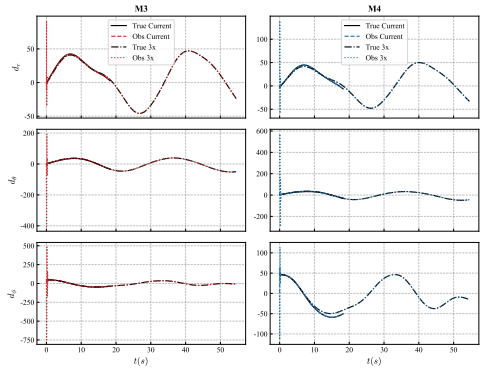
Table 4 quantifies this baseline performance. The terminal angle errors remain at the 10^{-6} level, the largest relative impact-speed error is 1.758×10^{-3} m/s, and the miss distance is approximately 0.88 m. These values verify the terminal speed and angle constraints, but the case also shows that terminal accuracy alone is insufficient for safe cooperative operation.



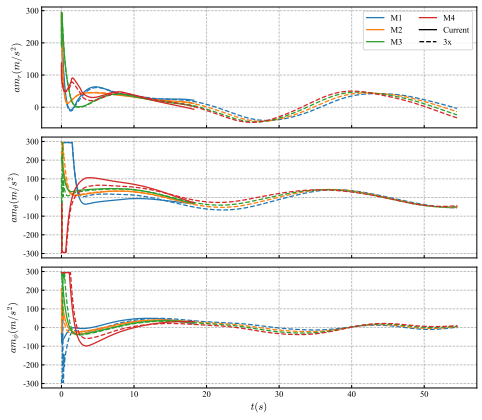
(**a**) Interception trajectories



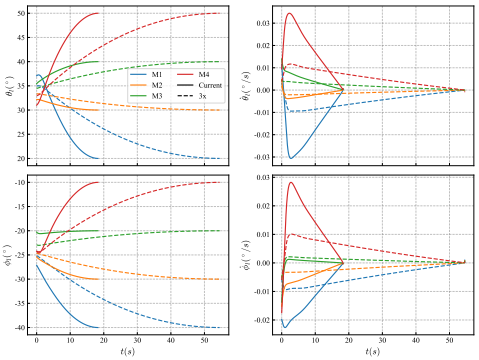
(**b**) Observation results of M1 and M2



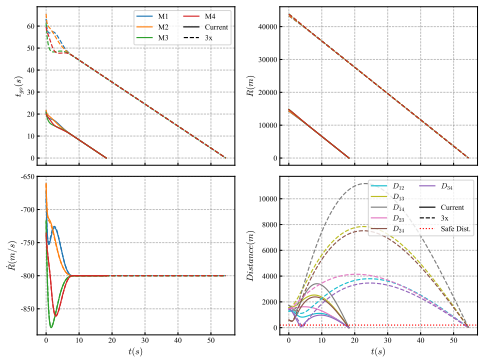
(**c**) Observation results of M3 and M4



(**d**) Accelerations



(**e**) LOS angles and LOS angular rates



(**f**) States and inter-vehicle distances

Figure 4. Baseline results with impact-speed regulation under the nominal and three-times-distance conditions.

Table 4. Baseline terminal errors with impact-speed regulation at the nominal initial distance.

Vehicle	Miss (m)	$\dot{R}$ Error (m/s)	θ_L Error (°)	ϕ_L Error (°)
M1	0.886	1.757×10^{-3}	2.107×10^{-6}	3.093×10^{-6}
M2	0.883	1.757×10^{-3}	2.046×10^{-6}	2.820×10^{-6}
M3	0.886	1.756×10^{-3}	1.917×10^{-6}	2.541×10^{-6}
M4	0.885	1.758×10^{-3}	1.690×10^{-6}	1.825×10^{-6}

Table 5 further reports the quantitative results under the three-times-distance condition. When the engagement duration increases from approximately 18–20 s under the nominal condition to approximately 55 s, the maximum terminal LOS-angle error does not exceed 5.381×10^{-5} deg, the maximum relative impact-speed error is 3.141×10^{-4} m/s, and the miss distances range from 0.325 to 0.385 m. These results show that the method retains stable terminal-constraint performance over the longer engagement. Together with the inter-vehicle spacing in Figure 4, the nominal condition also shows that high terminal accuracy alone is insufficient to guarantee safety during cooperative operation.

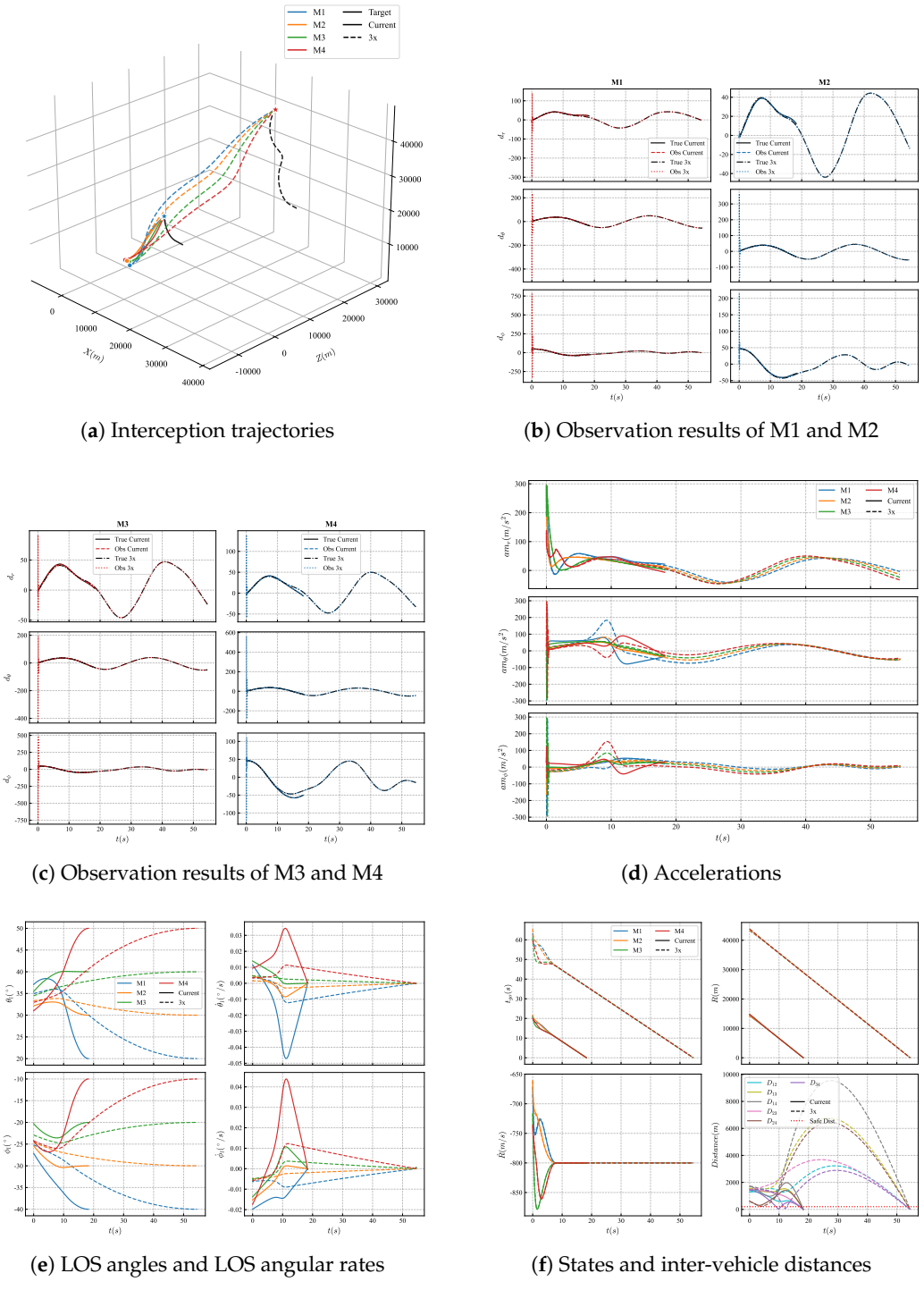
Table 5. Baseline terminal errors with impact-speed regulation under the three-times-distance condition.

Vehicle	Miss (m)	$\dot{R}$ Error (m/s)	θ_L Error (°)	ϕ_L Error (°)
M1	0.376	3.112×10^{-4}	9.414×10^{-8}	5.381×10^{-5}
M2	0.385	3.141×10^{-4}	1.277×10^{-5}	4.584×10^{-5}
M3	0.325	3.100×10^{-4}	2.772×10^{-5}	3.618×10^{-5}
M4	0.368	3.132×10^{-4}	4.236×10^{-5}	2.340×10^{-5}

4.2. Adaptive Transverse Control with Impact-Speed Regulation

The second case adds the adaptive reaching factor in the two angular channels, while the separation term remains inactive. Figure 5 uses the same solid–dashed convention for the nominal and three-times-distance conditions. The observer response in Figure 5b,c is still accurate after the initial transient, and Figure 5a,e,f show that the terminal speed and angle requirements are preserved. The main difference appears in Figure 5d: the early saturation of the transverse acceleration commands disappears. At the start of the engagement, the adaptive factor lowers the effective reaching gain and slows the angular-error response, which reduces the peak command. As the range decreases and the angular error becomes smaller, the gain increases and the terminal-angle constraint is recovered. Hence, the adaptive reaching law improves command smoothness without degrading terminal accuracy. However, Figure 5f also shows that the distance between Vehicle 3 and

Vehicle 4 decreases further, confirming that command smoothing alone does not solve the spacing problem. Under the three-times-distance condition, the sustained early saturation is likewise suppressed, but the spacing problem remains.



(**a**) Interception trajectories

(**b**) Observation results of M1 and M2

(**c**) Observation results of M3 and M4

(**d**) Accelerations

(**e**) LOS angles and LOS angular rates

(**f**) States and inter-vehicle distances

Figure 5. Adaptive transverse-control results under the nominal and three-times-distance conditions.

Table 6 gives the terminal errors of the adaptive transverse controller under the nominal initial-distance condition. The four vehicles have miss distances of 0.849–0.859 m and a maximum relative impact-speed error of 1.754×10^{-3} m/s; the maximum terminal LOS-angle error does not exceed 4.358×10^{-6} deg. These metrics are comparable to those in Table 4; together with Figure 5, they show that the adaptive law suppresses early overload saturation while essentially maintaining terminal accuracy.

Table 6. Terminal errors for adaptive transverse control at the nominal initial distance.

Vehicle	Miss (m)	$\dot{R}$ Error (m/s)	θ_L Error (°)	ϕ_L Error (°)
M1	0.859	1.751×10^{-3}	4.358×10^{-6}	1.202×10^{-6}
M2	0.852	1.752×10^{-3}	4.204×10^{-6}	1.239×10^{-6}
M3	0.849	1.753×10^{-3}	3.919×10^{-6}	1.307×10^{-6}
M4	0.857	1.754×10^{-3}	3.421×10^{-6}	1.256×10^{-6}

Table 7 further reports the results under the three-times-distance condition. When the engagement duration increases from approximately 18–20 s under the nominal condition to approximately 55 s, the four vehicles have miss distances of 0.344–0.366 m and a maximum relative impact-speed error of 3.138×10^{-4} m/s; the maximum terminal LOS-angle error does not exceed 5.756×10^{-5} deg. Compared with the nominal condition, the terminal LOS-angle error increases, but the miss distances and relative impact-speed error do not deteriorate, indicating that the adaptive controller retains small terminal errors over the longer engagement in this case.

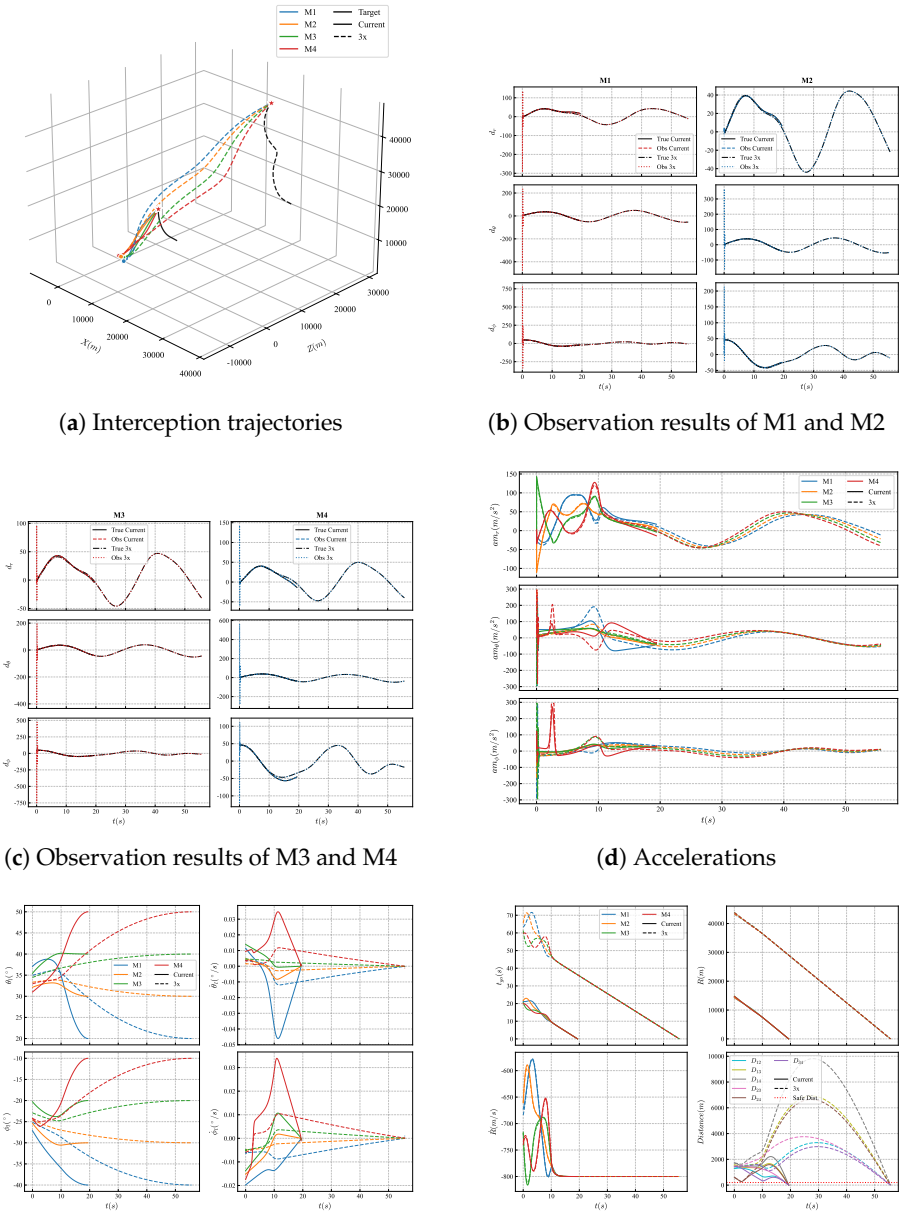
Table 7. Terminal errors for adaptive transverse control under the three-times-distance condition.

Vehicle	Miss (m)	$\dot{R}$ Error (m/s)	θ_L Error (°)	ϕ_L Error (°)
M1	0.348	3.108×10^{-4}	1.030×10^{-7}	5.756×10^{-5}
M2	0.354	3.138×10^{-4}	1.374×10^{-5}	4.903×10^{-5}
M3	0.366	3.097×10^{-4}	2.974×10^{-5}	3.870×10^{-5}
M4	0.344	3.129×10^{-4}	4.540×10^{-5}	2.502×10^{-5}

4.3. Adaptive Control with Two-Phase Separation

The third case activates the two-phase separation strategy in addition to the adaptive transverse controller. Figure 6 compares the nominal and three-times-distance conditions using solid and dashed curves, respectively. The observer response in Figure 6b,c is not degraded by the added transverse bias. The trajectories, LOS angles, and state histories in Figure 6a,e,f show that the multi-vehicle system still reaches the target with the assigned terminal geometry and impact-speed behavior. The acceleration histories in Figure 6d remain unsaturated, indicating that the separation command is compatible with the adaptive reaching law. With the two-phase separation strategy active, Figure 6f shows that, under the nominal condition, the inter-vehicle distance stays above 200 m before 12.88 s, and the distance margin is larger than those in Sections 4.1 and 4.2. Before 12.88 s, the repulsive bias governs the separation behavior. After the LOS angle errors enter the switching band, the vehicles proceed with different approach directions, so the later reduction in distance does not create a trajectory-crossing event. This result supports the intended division of safety functions between the two phases. Under the three-times-distance condition, Figure 6f likewise shows early repulsive separation followed by approach along differentiated terminal directions.

Table 8 gives the terminal results after introducing the two-phase separation strategy under the nominal initial-distance condition. The four vehicles have miss distances of 0.835–0.865 m and a maximum relative impact-speed error of 1.764×10^{-3} m/s; the maximum terminal LOS-angle error does not exceed 3.900×10^{-6} deg. These values are comparable to those in Table 6. Together with Figure 6, the results show that the two-phase separation strategy increases the early-stage inter-vehicle spacing without noticeably degrading terminal accuracy.



(**a**) Interception trajectories

(**b**) Observation results of M1 and M2

(**c**) Observation results of M3 and M4

(**d**) Accelerations

(**e**) LOS angles and LOS angular rates

(**f**) States and inter-vehicle distances

Figure 6. Adaptive control with two-phase separation under the nominal and three-times-distance conditions.

Table 8. Terminal errors for adaptive control with two-phase separation at the nominal initial distance.

Vehicle	Miss (m)	$\dot{R}$ Error (m/s)	θ_L Error (°)	ϕ_L Error (°)
M1	0.835	1.761×10^{-3}	3.900×10^{-6}	1.028×10^{-6}
M2	0.865	1.762×10^{-3}	3.770×10^{-6}	1.048×10^{-6}
M3	0.842	1.763×10^{-3}	3.515×10^{-6}	1.097×10^{-6}
M4	0.864	1.764×10^{-3}	3.086×10^{-6}	9.998×10^{-7}

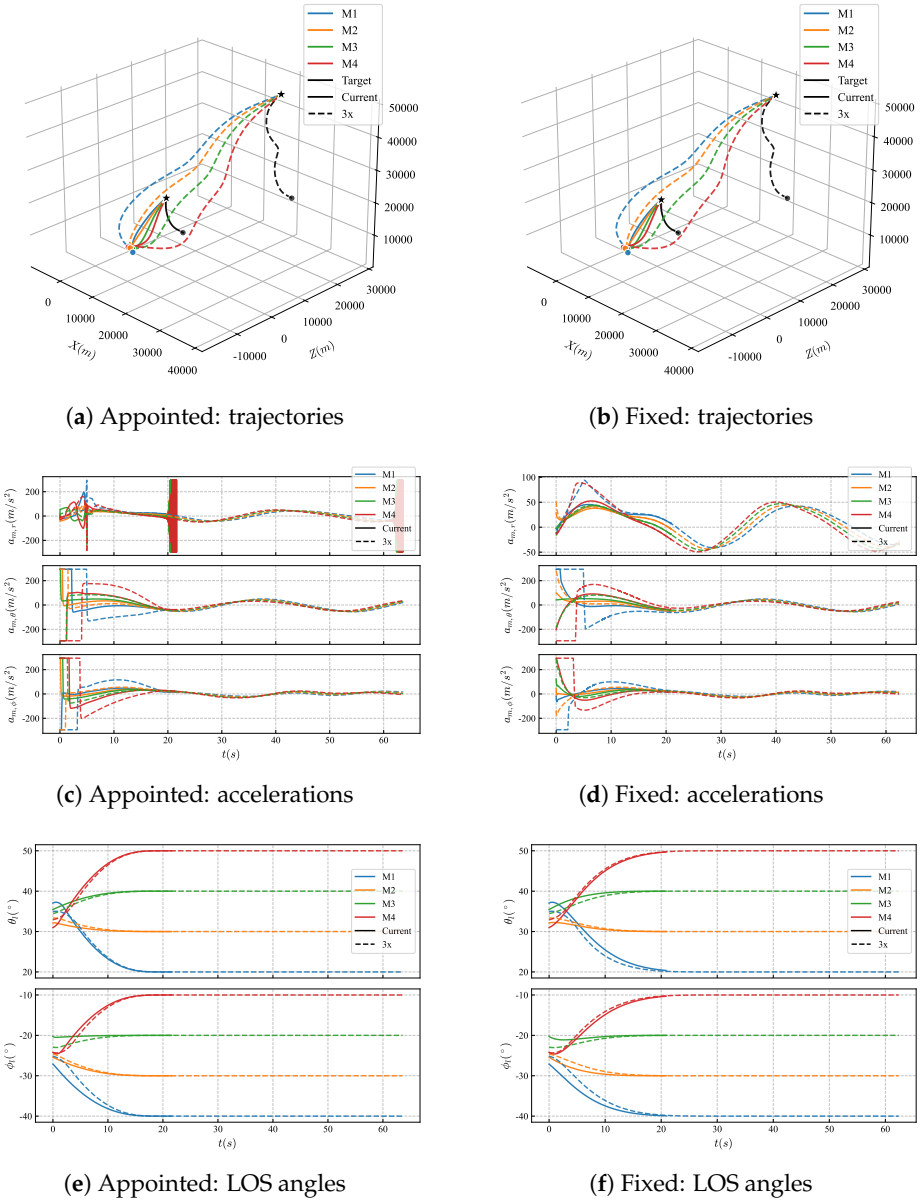
Table 9 further reports the results under the three-times-distance condition. When the engagement duration increases from approximately 18–20 s under the nominal condition to approximately 55 s, the four vehicles have miss distances of 0.368–0.377 m and a maximum relative impact-speed error of 4.493×10^{-4} m/s; the maximum terminal LOS-angle error does not exceed 6.511×10^{-5} deg. These metrics are on the same order as those in Table 7, indicating that introducing the two-phase separation strategy causes no noticeable loss of terminal accuracy over the longer engagement in this case.

Table 9. Terminal errors for adaptive control with two-phase separation under the three-times-distance condition.

Vehicle	Miss (m)	$\dot{R}$ Error (m/s)	θ_L Error (°)	ϕ_L Error (°)
M1	0.371	4.450×10^{-4}	2.404×10^{-5}	5.320×10^{-5}
M2	0.374	4.493×10^{-4}	3.830×10^{-5}	4.323×10^{-5}
M3	0.368	4.436×10^{-4}	5.261×10^{-5}	3.117×10^{-5}
M4	0.377	4.481×10^{-4}	6.511×10^{-5}	1.539×10^{-5}

4.4. Comparison with Existing Cooperative Laws

To assess command demand and terminal performance against representative time-constrained cooperative designs, the appointed-time law [62] and the fixed-time terminal-angle law [53] are selected as benchmarks. Figure 7 retains the nominal histories as solid curves and adds the three-times-distance histories as dashed curves.



(**a**) Appointed: trajectories (**b**) Fixed: trajectories

(**c**) Appointed: accelerations (**d**) Fixed: accelerations

(**e**) Appointed: LOS angles (**f**) Fixed: LOS angles

Figure 7. Benchmark results under the nominal and three-times-distance conditions. Note: The stars in subfigures (**a**,**b**) mark the interception points.

Figure 7 shows that both benchmark laws guide all four vehicles to the target, but their transient and terminal behavior differs. The appointed-time law exhibits terminal-phase chatter in its LOS-direction command. The fixed-time terminal-angle law undergoes prolonged acceleration-command saturation early in the guidance phase, and this prolonged saturation is not caused by the observer. By contrast, the proposed law exhibits only brief, mild saturation initially because of the relatively large initial estimation error of the FPESO; this saturation disappears as the estimation error rapidly converges.

Table 10 compares the descriptive metrics of the three methods under the nominal condition. The proposed law has a peak resultant overload of 29.53, lower than 42.80 for the appointed-time law and 36.44 for the fixed-time terminal-angle law. Its maximum terminal LOS-angle error is 3.900×10^{-6} deg, its miss distance is 0.865 m, and its relative impact-speed error is 1.764×10^{-3} m/s, all lower than the corresponding benchmark values. Neither benchmark law includes the independent radial relative-speed regulation loop used by the proposed law; therefore, their terminal relative impact-speed errors are substantially larger. Thus, under this condition, the proposed law reduces the peak command demand while retaining small terminal errors.

Table 11 gives the comparison under the three-times-distance condition. When the engagement duration increases from approximately 18–20 s under the nominal condition to approximately 55 s, the proposed law has a peak resultant overload of 44.53, which is lower than 44.66 for the appointed-time law but higher than 43.03 for the fixed-time terminal-angle law; it therefore no longer gives the lowest peak. Its maximum terminal LOS-angle error is 6.51×10^{-5} deg, smaller than 2.20×10^{-3} deg for the appointed-time law but larger than 2.08×10^{-6} deg for the fixed-time terminal-angle law. The proposed law has a miss distance of 0.38 m and a relative impact-speed error of 4.49×10^{-4} m/s, both lower than the corresponding benchmark values. Thus, over the longer engagement, its advantage lies mainly in miss distance and relative impact-speed regulation rather than in peak resultant overload or every terminal-angle metric.

Table 10. Descriptive metrics for the three cooperative guidance methods at the nominal initial distance.

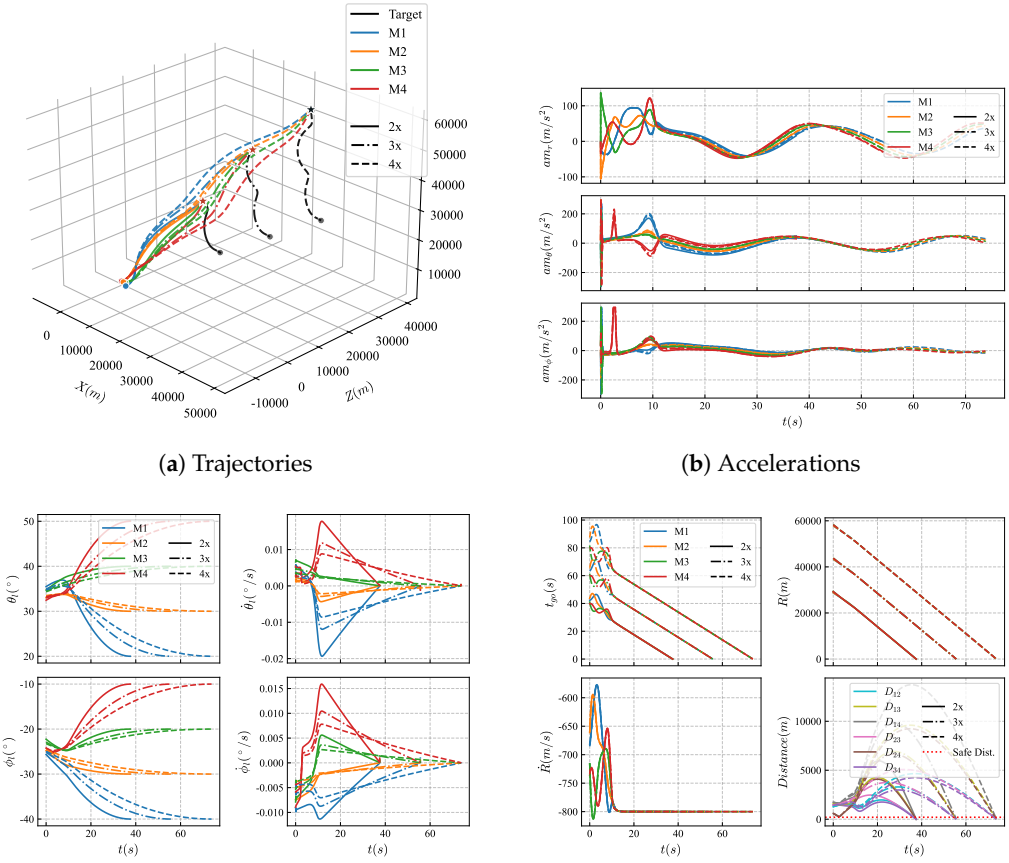
Method	Peak Resultant Overload	Miss (m)	$\dot{R}$ Error (m/s)	θ_L Error (°)	ϕ_L Error (°)
Appointed-time law [62]	42.80	1.06	124.43	5.57×10^{-4}	9.87×10^{-4}
Fixed-time terminal-angle law [53]	36.44	0.93	113.32	3.61×10^{-1}	3.09×10^{-1}
Proposed law	29.53	0.865	1.764×10^{-3}	3.900×10^{-6}	1.097×10^{-6}

Table 11. Descriptive metrics for the three cooperative guidance methods under the three-times-distance condition.

Method	Peak Resultant Overload	Miss (m)	$\dot{R}$ Error (m/s)	θ_L Error (°)	ϕ_L Error (°)
Appointed-time law [62]	44.66	0.92	90.90	2.20×10^{-3}	9.01×10^{-4}
Fixed-time terminal-angle law [53]	43.03	0.98	105.06	1.85×10^{-6}	2.08×10^{-6}
Proposed law	44.53	0.38	4.49×10^{-4}	6.51×10^{-5}	5.32×10^{-5}

4.5. Extended Initial-Distance Tests

To examine whether terminal performance is maintained as the guidance interval increases, the initial vehicle–target distances are scaled by factors of 2, 3, and 4, with the remaining settings unchanged. The engagement duration is jointly determined by the initial distance, closing speed, and encounter geometry; Figure 8 presents the trajectories, acceleration commands, and LOS-angle responses for the two-, three-, and four-times-distance conditions, while Table 12 summarizes their terminal performance.



(**a**) Trajectories (**b**) Accelerations

(**c**) LOS-angle convergence (**d**) States and inter-vehicle distances

Figure 8. Extended initial-distance results for the two-, three-, and four-times-distance conditions. Note: The stars in subfigure (**a**) mark the interception points for the two-, three-, and four-times-distance conditions.

Table 12. Performance under extended initial vehicle–target distances.

Initial-Distance Scale	Approx. Duration (s)	θ_L Error (°)	ϕ_L Error (°)	Miss (m)	$\dot{R}$ Error (m/s)
2×	≈38	2.34×10^{-6}	2.31×10^{-5}	0.74	1.83×10^{-3}
3×	≈55	6.51×10^{-5}	5.32×10^{-5}	0.38	4.49×10^{-4}
4×	≈75	2.28×10^{-7}	6.22×10^{-7}	0.90	1.91×10^{-4}

Figure 8 shows that the main behavior observed in the preceding deterministic cases is retained under the two-, three-, and four-times-distance conditions. The four vehicles follow distinct trajectories during the extended approach and converge at the target. After the initial transient, the acceleration commands in all three conditions stay within the imposed limit and vary smoothly; meanwhile, the LOS angles approach their assigned terminal values and the angular rates decay toward zero.

Table 12 summarizes terminal performance at two, three, and four times the initial distance, with engagement durations of approximately 38, 55, and 75 s, respectively. The maximum terminal LOS-angle errors in all three conditions do not exceed 6.51×10^{-5} deg, the relative impact-speed errors range from 1.91×10^{-4} to 1.83×10^{-3} m/s, and the miss distances range from 0.38 to 0.90 m. Across the three tested distance scales, these metrics do not deteriorate monotonically as the engagement duration increases, indicating that the proposed law retains small terminal errors.

4.6. Monte Carlo Simulation Tests

Monte Carlo tests were performed in two groups to evaluate sensitivity to launch-condition or target-state perturbations and measurement noise.

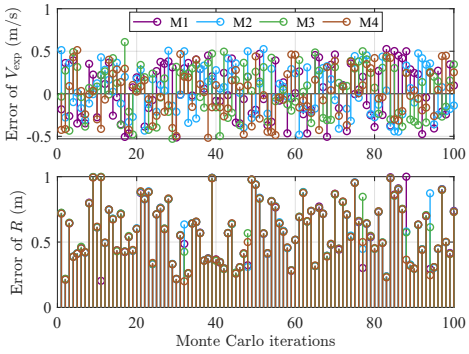
(1) The target initial state was fixed, and the interceptor launch states were perturbed.

The interceptor position errors were drawn uniformly from $[-100, 100]$ m, and the speed errors were drawn from $[-10, 10]$ m/s. Initial flight-path elevation and azimuth errors were drawn from $[-5°, 5°]$. The prescribed relative speed V_{exp} was varied in $[-1000, -800]$ m/s, and the desired LOS inclination and declination angles were also perturbed within $[-5°, 5°]$. Zero-mean Gaussian noise was added at levels of 1 m/s in $\dot{R}$ and 0.005 rad/s in $\dot{\phi}_{L,i}$ and $\dot{\theta}_{L,i}$. A run stopped once $R < 1$ m and $\dot{R} > 0$.

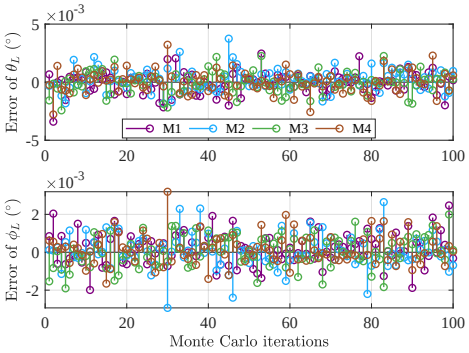
(2) The interceptor launch states were fixed, and the target initial state was perturbed.

Target position, speed, flight-path elevation, and flight-path azimuth errors used the same ranges as the first group. The desired terminal angles remained unchanged.

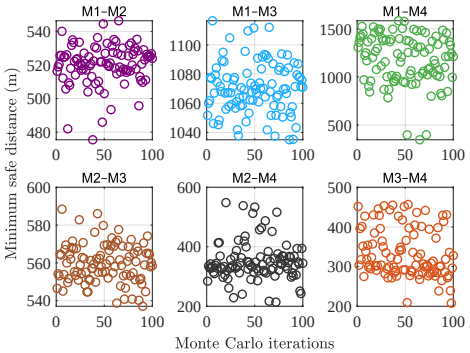
Each analysis set contained 200 records. For each record, the minimum of all six pairwise distances over 0–15 s was used as the spacing metric. To avoid excessive visual overlap, Figures 9 and 10 separately display the first 100 records of the launch-state and target-state sets in their fixed stored order, whereas Tables 13 and 14 report summary statistics for the corresponding 200-record analysis sets.



(**a**) Speed error and miss distance



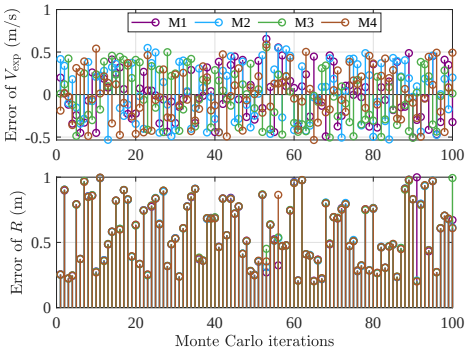
(**b**) Angle errors



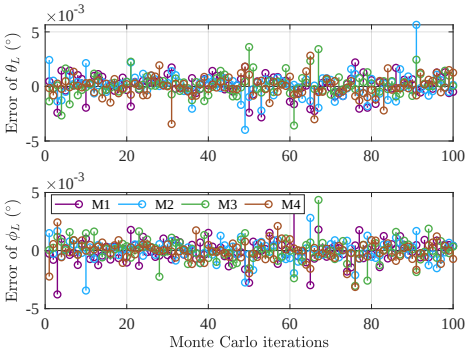
(**c**) Minimum spacing

Figure 9. Launch-state perturbation results for the first 100 records of the 200-record set.

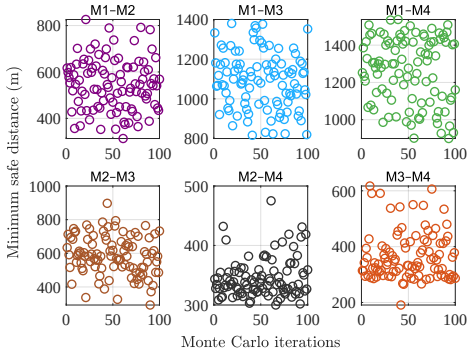
Figure 9a–c show successful interception in all sampled launch-condition cases. The miss distances cluster near 0.5 m, and the terminal angle errors remain at the 10^{-3} level despite measurement noise. The vehicles also converge to their assigned approach directions. The minimum-distance plot in Figure 9c stays above the prescribed 200 m threshold, indicating that the two-phase strategy preserves internal separation with these perturbations. The statistics in Table 13 are consistent with the trends observed in Figure 9 and further quantify the terminal accuracy and inter-vehicle spacing over all 200 records.



(**a**) Speed error and miss distance



(**b**) Angle errors



(**c**) Minimum spacing

Figure 10. Target-state perturbation results for the first 100 records of the 200-record set.

Table 13. Monte Carlo statistics for the launch-state perturbation set (200 records).

Metric	Mean ± SD	Worst Recorded
$\lvert\theta_L\rvert$ error (°)	$6.95 \times 10^{-4} \pm 6.05 \times 10^{-4}$	4.00×10^{-3}
$\lvert\phi_L\rvert$ error (°)	$6.98 \times 10^{-4} \pm 6.79 \times 10^{-4}$	8.57×10^{-3}
Absolute relative-speed error (m/s)	0.246 ± 0.147	0.608
Miss distance (m)	0.591 ± 0.221	0.999
Minimum spacing, 0–15 s (m)	297.57 ± 31.47	201.84

Note: Terminal rows pool the recorded four-vehicle terminal outputs; the spacing row uses one six-pair minimum from each of the 200 records.

Table 14. Monte Carlo statistics for the target-state perturbation set (200 records).

Metric	Mean ± SD	Worst Recorded
$\lvert\theta_L\rvert$ error (°)	$7.35 \times 10^{-4} \pm 6.74 \times 10^{-4}$	5.65×10^{-3}
$\lvert\phi_L\rvert$ error (°)	$7.06 \times 10^{-4} \pm 6.61 \times 10^{-4}$	4.36×10^{-3}
Absolute relative-speed error (m/s)	0.258 ± 0.152	0.841
Miss distance (m)	0.598 ± 0.240	0.9999
Minimum spacing, 0–15 s (m)	315.12 ± 24.24	190.88

Note: Terminal rows pool the recorded four-vehicle terminal outputs; the spacing row uses one six-pair minimum from each of the 200 records.

Figure 10a–c demonstrate that target-state perturbations do not prevent cooperative interception. The miss distances again remain near 0.5 m, and the terminal constraint errors stay within the same order as in the first group. The statistics in Table 14 are consistent with the trends observed in Figure 10 and further quantify the terminal accuracy and inter-vehicle spacing over all 200 records.

Taken together, the simulations indicate that the proposed method reduces initial overload demand, smooths the control input, and increases the minimum inter-vehicle distance while preserving terminal angle and relative impact-speed accuracy in the tested scenarios.

5. Conclusions

This study addressed cooperative engagements in which arrival coordination, terminal geometry, impact-speed regulation, and internal spacing must be satisfied together. The radial command combines range consensus with a common relative impact-speed loop, so that inter-vehicle difference dynamics and the group-average closing-speed mode are handled separately. The two angular commands use an adaptive reaching law whose gain depends on time, sliding-state magnitude, and remaining range. A two-phase separation mechanism is then added: transverse repulsion is used before terminal angle convergence, and differentiated approach directions maintain separation after convergence.

The deterministic simulations clarify the role of each component. The radial controller keeps the remaining range and radial velocity synchronized while driving the average radial velocity toward V_{exp}. The adaptive transverse controller suppresses the early overload saturation observed in the fixed-gain case and produces smoother control inputs. After the two-phase separation mechanism is introduced, the minimum inter-vehicle distance increases without noticeable loss of terminal performance. Across the three ablation cases, both the nominal and three-times-distance conditions retain the terminal angle and relative impact-speed constraints, and all miss distances remain below 0.9 m. The benchmark comparison further shows that the proposed law maintains terminal geometry and relative impact-speed regulation under the tested conditions.

The extended initial-distance tests further examined engagement durations of approximately 38, 55, and 75 s. Across these cases, the command-smoothing behavior and terminal constraints are maintained over the tested distance scales. Two 200-run Monte Carlo tests further examined variations in the interceptor launch states or the target initial state under measurement noise conditions. In these tests, the terminal angle errors stay at the 10^{-3} level, while the relative impact-speed errors and miss distances remain below 1 m/s and 1 m, respectively. These results suggest that the proposed law can reduce command demand and maintain terminal accuracy over the tested conditions. The deterministic ablation cases also show that the two-phase separation mechanism increases the internal distance margin.

Future outlook: The separation strategy proposed here is intended to increase the distance margin for the studied cooperative configurations. Because the artificial potential field is local, it does not provide a formal global safety guarantee when several neighboring vehicles impose conflicting avoidance directions. The local separation mechanism can be further extended by combining barrier-Lyapunov functions with constrained optimization for multi-neighbor encounters. Communication delay, packet loss, and switching topologies will also be considered when the framework is extended to networked guidance.

Author Contributions: Conceptualization, S.Y.; methodology, S.Y. and Z.G.; software, S.Y.; validation, S.Y.; formal analysis, S.Y.; writing—original draft, S.Y.; writing—review and editing, Z.G. and W.Y.; supervision, Z.G. and W.Y.; project administration, Z.G.; funding acquisition, W.Y. All authors have read and agreed to the published version of the manuscript.

Funding: This work was supported by the National Natural Science Foundation of China (Grant No. 62203191), the National Defence Key Laboratory of Science and Technology (Grant No. 2022JCJQLB06105), the Basic Science (Natural Science) Research Projects in Higher Education Institutions (Grant No. 22KJB590001), the China Postdoctoral Science Foundation (Grant No. 2024M754148), Program of China Scholarship Council (Grant No. 202506840167), and the Postdoctoral Fellowship Program (Grade B) of China Postdoctoral Science Foundation (Grant No. GZB20240980).

Institutional Review Board Statement: Not applicable.

Informed Consent Statement: Not applicable.

Data Availability Statement: Data are contained within the article.

Conflicts of Interest: The authors declare no conflicts of interest or personal relationships that could have appeared to influence the work reported in this paper.

References

1. Zhao, S.; Zhou, R. Cooperative guidance for multimissile salvo attack. *Chin. J. Aeronaut.* **2008**, *21*, 533–539. [CrossRef]
2. Yu, J.; Dong, X.; Li, Q.; Ren, Z.; Lv, J. Cooperative guidance strategy for multiple hypersonic gliding vehicles system. *Chin. J. Aeronaut.* **2020**, *33*, 990–1005. [CrossRef]
3. Liu, S.; Yan, B.; Zhang, T.; Dai, P.; Liu, R.; Yan, J. Three-dimensional cooperative guidance law for intercepting hypersonic targets. *Aerosp. Sci. Technol.* **2022**, *129*, 107815. [CrossRef]
4. Feng, R.; Liu, S.; Huang, W.; Han, T.; Yan, B.; Wang, Z.; Niu, Y. Bridging game theory and multi-agent systems: Development status and future prospects. *Prog. Aerosp. Sci.* **2026**, *161*, 101183. [CrossRef]
5. Yang, Q.; Liu, S.; Wu, X.; Han, T.; Shin, H.S.; Tekin, R. A review of trajectory planning for high speed vehicles: Current advancements and future prospects. *Aerosp. Sci. Technol.* **2026**, *176*, 112667. [CrossRef]
6. You, H.; Chang, X.; Zhao, J.; Wang, S.; Zhang, Y. Three-dimensional impact-angle-constrained cooperative guidance strategy against maneuvering target. *ISA Trans.* **2023**, *138*, 262–280. [CrossRef] [PubMed]
7. Wang, Z.; Fu, W.; Fang, Y.; Zhu, S.; Wu, Z.; Wang, M. Prescribed-time cooperative guidance law against maneuvering target based on leader-following strategy. *ISA Trans.* **2022**, *129*, 257–270. [CrossRef] [PubMed]
8. Zhan, Y.; Li, S.; Zhou, D. Time-to-go based three-dimensional multi-missile spatio-temporal cooperative guidance law: A novel approach for maneuvering target interception. *ISA Trans.* **2024**, *149*, 178–195. [CrossRef] [PubMed]
9. You, H.; Chang, X.; Zhao, J.; Wang, S.; Zhang, Y. Three-dimensional impact-angle-constrained fixed-time cooperative guidance algorithm with adjustable impact time. *Aerosp. Sci. Technol.* **2023**, *141*, 108574 . [CrossRef]
10. Wang, X.; Lu, X. Three-dimensional impact angle constrained distributed guidance law design for cooperative attacks. *ISA Trans.* **2018**, *73*, 79–90. [CrossRef] [PubMed]
11. Tahk, M.J.; Shim, S.W.; Hong, S.M.; Choi, H.L.; Lee, C.H. Impact time control based on time-to-go prediction for sea-skimming antiship missiles. *IEEE Trans. Aerosp. Electron. Syst.* **2018**, *54*, 2043–2052. [CrossRef]
12. Lyu, T.; Guo, Y.; Li, C.; Ma, G.; Zhang, H. Multiple missiles cooperative guidance with simultaneous attack requirement under directed topologies. *Aerosp. Sci. Technol.* **2019**, *89*, 100–110. [CrossRef]
13. Zhao, J.; Yang, S. Integrated cooperative guidance framework and cooperative guidance law for multi-missile. *Chin. J. Aeronaut.* **2018**, *31*, 546–555. [CrossRef]
14. Zhang, Y.; Wang, X.; Wu, H. A distributed cooperative guidance law for salvo attack of multiple anti-ship missiles. *Chin. J. Aeronaut.* **2015**, *28*, 1438–1450. [CrossRef]
15. Zhang, S.; Guo, Y.; Liu, Z.; Wang, S.; Hu, X. Finite-time cooperative guidance strategy for impact angle and time control. *IEEE Trans. Aerosp. Electron. Syst.* **2020**, *57*, 806–819. [CrossRef]
16. Wang, C.; Dong, W.; Wang, J.; Shan, J.; Xin, M. Guidance law design with fixed-time convergent error dynamics. *J. Guid. Control Dyn.* **2021**, *44*, 1389–1398. [CrossRef]
17. Hou, Z.; Yang, Y.; Liu, L.; Wang, Y. Terminal sliding mode control based impact time and angle constrained guidance. *Aerosp. Sci. Technol.* **2019**, *93*, 105142. [CrossRef]
18. Chen, Z.; Chen, W.; Liu, X.; Cheng, J. Three-dimensional fixed-time robust cooperative guidance law for simultaneous attack with impact angle constraint. *Aerosp. Sci. Technol.* **2021**, *110*, 106523. [CrossRef]
19. Liu, S.; Lin, Z.; Huang, W.; Yan, B. Technical development and future prospects of cooperative terminal guidance based on knowledge graph analysis: A review. *J. Zhejiang Univ.-Sci. A* **2025**, *26*, 605–634. [CrossRef]
20. Wang, C.; Wang, W.; Dong, W.; Wang, J.; Deng, F. Multiple-stage spatial–temporal cooperative guidance without time-to-go estimation. *Chin. J. Aeronaut.* **2024**, *37*, 399–416. [CrossRef]
21. Yu, C.; Zhu, B.; Zheng, J.; Wang, W. Three dimensional cooperative guidance for intercepting a manoeuvering target. *IET Control Theory Appl.* **2023**, *18*, 530–540. [CrossRef]
22. Wang, X.H.; Tan, C.P. 3-D impact angle constrained distributed cooperative guidance for maneuvering targets without angular-rate measurements. *Control Eng. Pract.* **2018**, *78*, 142–159. [CrossRef]
23. Li, H.; Wang, J.; Tao, H.; Lin, D. Near-optimal impact-vector-control guidance. *J. Guid. Control Dyn.* **2024**, *47*, 1965–1972. [CrossRef]
24. Huang, A.; Yu, J.; Liu, Y.; Wang, Y.; Hua, Y.; Dong, X. Prescribed time fully distributed guidance against maneuvering targets with performance constraints. *J. Frankl. Inst.* **2026**, *363*, 108602. [CrossRef]

25. Hou, L.; Luo, H.; Shi, H.; Shin, H.S.; He, S. An Optimal Geometrical Guidance Law for Impact Time and Angle Control. *IEEE Trans. Aerosp. Electron. Syst.* **2023**, *59*, 9821–9830. [CrossRef]
26. Wang, C.; Dong, W.; Wang, J.; Shan, J. Nonlinear suboptimal guidance law with impact angle constraint: An SDRE-based approach. *IEEE Trans. Aerosp. Electron. Syst.* **2020**, *56*, 4831–4840. [CrossRef]
27. Zhou, J.; Lü, Y.; Li, Z.; Yang, J. Cooperative guidance law design for simultaneous attack with multiple missiles against a maneuvering target. *J. Syst. Sci. Complex.* **2018**, *31*, 287–301. [CrossRef]
28. Li, G.; Li, Q.; Wu, Y.; Xu, P.; Liu, J. Leader-following cooperative guidance law with specified impact time. *Sci. China Technol. Sci.* **2020**, *63*, 2349–2356. [CrossRef]
29. Li, S.; Liu, J.; Negenborn, R.R. Distributed coordination for collision avoidance of multiple ships considering ship maneuverability. *Ocean Eng.* **2019**, *181*, 212–226. [CrossRef]
30. Liu, J.; Zhang, J.; Yan, X.; Soares, C.G. Multi-ship collision avoidance decision-making and coordination mechanism in Mixed Navigation Scenarios. *Ocean Eng.* **2022**, *257*, 111666. [CrossRef]
31. Huang, S.; Teo, R.S.H.; Tan, K.K. Collision avoidance of multi unmanned aerial vehicles: A review. *Annu. Rev. Control* **2019**, *48*, 147–164. [CrossRef]
32. Wang, X.; Shen, L.; Liu, Z.; Zhao, S.; Cong, Y.; Li, Z.; Jia, S.; Chen, H.; Yu, Y.; Chang, Y.; et al. Coordinated flight control of miniature fixed-wing UAV swarms: Methods and experiments. *Sci. China Inf. Sci.* **2019**, *62*, 1–17. [CrossRef]
33. Chen, S.; Ma, D.; Yao, Y.; Wang, X.; Li, C. Cooperative polynomial guidance law with collision avoidance and flight path angle coordination. *Aerosp. Sci. Technol.* **2022**, *130*, 107809. [CrossRef]
34. Chen, J.; Sun, R.; Lu, Y. Cooperative game penetration guidance for multiple hypersonic vehicles under safety critical framework. *Chin. J. Aeronaut.* **2024**, *37*, 247–255. [CrossRef]
35. Gao, Z.; Liu, J.; Huang, J.; Wang, W.; Yi, W.; Yuan, S. Three-dimensional fault-tolerant cooperative guidance law with constraints on relative impact velocity and attack angle. *Aerosp. Sci. Technol.* **2026**, *168*, 111003. [CrossRef]
36. Li, Y.; Zhu, M.; An, B.; Zhi, Y.; Liu, L.; Fan, H.; Wang, B. Three-dimensional cooperative guidance laws with impact velocity and impact angles constraints. *Aerosp. Sci. Technol.* **2025**, *159*, 109997. [CrossRef]
37. Wang, Y.; Li, R.; Wu, Z.; Chen, K.; Yu, D. Precise impact time and angle guidance strategy under time-varying velocity. *Nonlinear Dyn.* **2024**, *112*, 10109–10125. [CrossRef]
38. Yang, Z.; Liu, X.; Liu, H. Impact time control guidance law with time-varying velocity based on deep reinforcement learning. *Aerosp. Sci. Technol.* **2023**, *142*, 108603. [CrossRef]
39. Zhang, W.; Chen, W.; Li, J.; Yu, W. Guidance algorithm for impact time, angle, and acceleration control under varying velocity condition. *Aerosp. Sci. Technol.* **2022**, *123*, 107462. [CrossRef]
40. Sun, G.; Wen, Q.; Xu, Z.; Xia, Q. Impact time control using biased proportional navigation for missiles with varying velocity. *Chin. J. Aeronaut.* **2020**, *33*, 956–964. [CrossRef]
41. Huang, A.; Wang, X.; Zhao, Q.; Yu, J.; Dong, X. Three-dimensional practical cooperative guidance law for salvo attack considering velocity variation. *Aerosp. Sci. Technol.* **2025**, *166*, 110588. [CrossRef]
42. Shi, P.; Yu, J.; Xiwang, D.; Dong, X.; Li, Q.; Ren, Z. Distributed adaptive cooperative guidance against maneuvering targets with time-varying terminal angle constraint and overload saturation. *J. Frankl. Inst.* **2023**, *360*, 11507–11528. [CrossRef]
43. Shen, H.; Jiang, H.; Cai, Y.; Deng, Y. Three-dimensional prescribed-time cooperative guidance with neural network-based disturbance observer and LOS constraint. *Control Eng. Pract.* **2025**, *165*, 106599. [CrossRef]
44. Zhao, K.; Song, J.; Yu, J.; Liu, Y. Cooperative guidance under multiple constraints without active speed control. *Aerosp. Sci. Technol.* **2025**, *164*, 110446. [CrossRef]
45. Lan, X.; Yan, J.; Zhao, Z.; Zou, T. Three-Dimensional Self-Learning Optimal Collaborative Guidance Strategy for Multimissile Salvo Attacks on Variable Maneuvering Target. *IEEE Trans. Aerosp. Electron. Syst.* **2025**, *61*, 11781–11794. [CrossRef]
46. Gu, H.H.; Wang, R.Z.; Tang, M.J.; Zhang, X.C.; Tu, S.T. Data-physics-model based fatigue reliability assessment methodology for high-temperature components and its application in steam turbine rotor. *Reliab. Eng. Syst. Saf.* **2024**, *241*, 109633. [CrossRef]
47. Song, L.K.; Tao, F.; Li, X.Q.; Yang, L.C.; Wei, Y.P.; Beer, M. Physics-embedding multi-response regressor for time-variant system reliability assessment. *Reliab. Eng. Syst. Saf.* **2025**, *263*, 111262. [CrossRef]
48. Song, L.K.; Faes, M.G.R.; Tao, F. Generative data-physics fusion for hierarchical reliability assessment. *Reliab. Eng. Syst. Saf.* **2026**, *272*, 112642. [CrossRef]
49. Wu, T.; Wang, Z.; Wei, C.; Ning, X.; Chen, Z. Adaptive fixed-time fuzzy fault-tolerant cooperative spiral-diving guidance law with initial state-independent prescribed performance. *Chin. J. Aeronaut.* **2025**, *39*, 103975. [CrossRef]
50. Wu, Z.; Feng, W.; Zhang, X.; Fu, W.; Ren, Z.; Han, T. Three-dimensional cooperative guidance law with practical predefined-time approach angle and time-to-go convergence. *Chin. J. Aeronaut.* **2025**, *39*, 103960. [CrossRef]
51. Du, X.; Yang, G. Event-triggered distributed cooperative guidance by multiple-leaders-followers strategy. *J. Frankl. Inst.* **2025**, *362*, 108165. [CrossRef]

52. Liu, Y.; Yu, D.; Jia, Q. Dynamic event-triggered prescribed-time cooperative guidance law for salvo attack with impact angle constraints. *Aerosp. Sci. Technol.* **2026**, *168*, 110873. [CrossRef]
53. Dong, W.; Wang, C.; Wang, J.; Zuo, Z.; Shan, J. Fixed-Time Terminal Angle-Constrained Cooperative Guidance Law Against Maneuvering Target. *IEEE Trans. Aerosp. Electron. Syst.* **2022**, *58*, 1352–1366. [CrossRef]
54. Ni, J.; Liu, L.; Liu, C.; Liu, J. Fixed-Time Leader-Following Consensus for Second-Order Multiagent Systems with Input Delay. *IEEE Trans. Ind. Electron.* **2017**, *64*, 8635–8646. [CrossRef]
55. Wang, X.; Hong, Y. Finite-Time Consensus for Multi-Agent Networks with Second-Order Agent Dynamics. *IFAC Proc. Vol.* **2008**, *41*, 15185–15190. [CrossRef]
56. Jiang, S.; Tian, F.; Sun, S.; Liang, W. Integrated guidance and control of guided projectile with multiple constraints based on fuzzy adaptive and dynamic surface. *Def. Technol.* **2020**, *16*, 1130–1141. [CrossRef]
57. Liu, Y.; Xie, N.; Li, K.; Liang, Y. Missile guidance law design based on free-time convergent error dynamics. *J. Syst. Eng. Electron.* **2024**, *35*, 1315–1325. [CrossRef]
58. Surve, P.; Maity, A.; Kumar, S.R. Polynomial shaping based three-dimensional impact angle and field-of-view constrained guidance. *Aerosp. Sci. Technol.* **2024**, *147*, 109018. [CrossRef]
59. Zhan, Y.; Wang, L.; Zhou, D. Finite-time differential games in missile guidance: Achieving motion camouflage and robust cooperative encirclement guidance. *ISA Trans.* **2025**, *167*, 1520–1535. [CrossRef] [PubMed]
60. Liang, L.; Zhao, B.; Zhou, J.; Zhang, Z. Impact angle controlled integrated guidance and control with input and state constraints. *Int. J. Control* **2024**, *97*, 796–810. [CrossRef]
61. Wang, X.; Lu, H.; Huang, X.; Yang, Y.; Zuo, Z. Three-dimensional time-varying sliding mode guidance law against maneuvering targets with terminal angle constraint. *Chin. J. Aeronaut.* **2022**, *35*, 303–319. [CrossRef]
62. Zhang, L.; Li, D.; Jing, L.; Ju, X.; Cui, N. Appointed-Time Cooperative Guidance Law with Line-of-Sight Angle Constraint and Time-to-go Control. *IEEE Trans. Aerosp. Electron. Syst.* **2023**, *59*, 3142–3155. [CrossRef]

Disclaimer/Publisher's Note: The statements, opinions and data contained in all publications are solely those of the individual author(s) and contributor(s) and not of MDPI and/or the editor(s). MDPI and/or the editor(s) disclaim responsibility for any injury to people or property resulting from any ideas, methods, instructions or products referred to in the content.